Local Deformable 3D Reconstruction with Cartan's Connections

Shaifali Parashar, Daniel Pizarro, Adrien Bartoli

Local Deformable 3D Reconstruction with Cartan's Connections

Shaifali Parashar[1], Daniel Pizarro[2,1] and Adrien Bartoli[1]

[1]EnCoV - CNRS/Université d'Auvergne, Clermont-Ferrand, France
[2]GEINTRA, Universidad de Alcalá, Alcalá de Henares, Spain

Abstract—

3D reconstruction of deformable objects using inter-image visual motion from monocular images has been studied under Shape-from-Template (SfT) and Non-Rigid Structure-from-Motion (NRSfM). Most methods have been developed for simple deformation models, primarily isometry. They may treat a surface as a discrete set of points and draw constraints from the points only or they may use a non-parametric representation and use both points and differentials to express constraints. We propose a differential framework based on Cartan's theory of connections and moving frames. It is applicable to SfT and NRSfM, and to deformation models other than isometry. It utilises infinitesimal-level assumptions on the surface's geometry and mappings. It has the following properties. 1) It allows one to derive existing solutions in a simpler way. 2) It models SfT and NRSfM in a unified way. 3) It allows us to introduce a new skewless deformation model and solve SfT and NRSfM for it. 4) It facilitates a generic solution to SfT which does not require deformation modeling. Our framework is complete: it solves deformable 3D reconstruction for a whole class of algebraic deformation models including isometry. We compared our solutions with the state-of-the-art methods and show that ours outperform in terms of both accuracy and computation time.

1 Introduction

Reconstructing the 3D shape of objects from multiple images is an important goal in computer vision. It has been extensively studied for both rigid and deformable objects. While there are accurate and stable solutions such as Structure-from-Motion (SfM) for reconstructing the rigid objects (Hartley and Zisserman, 2000), the deformable case remains an open research problem. SfM relies on various concepts from projective geometry to draw constraints on the geometry of rigid objects. It fails on deformable objects as it cannot model the effect of deformations. Deformable 3D reconstruction refers to the techniques to reconstruct the deformable objects by taking into account the effect of deformation on the geometry of the object. It has been proposed with Shape-from-Template (SfT) (Bartoli et al., 2015; Chhatkuli et al., 2017b; Gumerov et al., 2004; Haouchine et al., 2014; Malti et al., 2013; Ngo et al., 2015; Perriollat et al., 2011; Salzmann and Fua, 2011) and Non-Rigid Structure-from-Motion (NRSfM) (Akhter et al., 2009; Bregler et al., 2000; Dai et al., 2014; Del Bue et al., 2004; Gotardo and Martinez, 2011; Torresani et al., 2008). SfT uses a single image along with a 3D template, which is a textured 3D shape of the object, whereas NRSfM requires multiple images from a single camera.

Other possible ways to recover the depth of deformable objects are by using an active sensor such as Kinect (Innmann et al., 2016; Newcombe et al., 2015; Zollhöfer et al., 2018), a synchronized system of multiple cameras (Cagniart et al., 2010; De Aguiar et al., 2008; Starck and Hilton, 2003) or machine learning (Mehta et al., 2018; Pumarola et al., 2018; Tewari et al., 2018; Zhou et al., 2018). The use of these approaches is however limited due to the constraints of accuracy, sensor, size and amount of training data required. This makes deformable 3D reconstruction from regular images a relevant research problem.

The deformable 3D reconstruction methods SfT and NRSfM both require deformation constraints. These are either *i)* statistics-based or *ii)* physics-based. *i)* restricts the underlying shape or trajectory of the object to lie in a low-rank space while *ii)* models the deformation by constraining the physical object properties. For *i)*, SfT uses a pre-trained low-rank shape model as template (Blanz and Vetter, 2003) while NRSfM recovers the shape (Bregler et al., 2000; Del Bue et al., 2004; Torresani et al., 2008) or trajectory bases (Akhter et al., 2009; Dai et al., 2014; Gotardo and Martinez, 2011) and deformation coefficients. *ii)* may use either a *mesh-based* or a *differential* framework. The mesh-based framework represents a surface with a mesh or a discrete neighborhood-aware point set. The differential framework uses a non-parametric and continuous surface representation where the surface differentials at a point are related to its local neighborhood.

Most methods in *ii)* use a simple deformation model called isometry, which preserves the geodesic distance between points on the object's surface. A piece of paper or unstretched cloth are typically isometric. Mesh-based SfT (Ngo et al., 2015; Perriollat et al., 2011; Salzmann and Fua, 2011) and NRSfM (Chhatkuli et al., 2017a; Taylor et al., 2010; Vicente and Agapito, 2012) reconstruct by using a convex relaxation of isometry, namely inextensibility. For non-isometric surfaces, mesh-based SfT (Haouchine et al., 2014; Moreno-Noguer et al., 2009) and NRSfM (Agudo and Moreno-Noguer, 2015; Agudo et al., 2016) use elasticity.

The elastic NRSfM methods also use a low-rank force model, thus combining *i)* and *ii)*. Under a differential framework, (Bartoli et al., 2015) proposed SfT to reconstruct both isometric and non-isometric surfaces by modeling isometric (distance-preserving) and conformal (angle-preserving) deformations respectively. It modeled both deformations using a metric tensor (MT), which expresses local metric quantities such as lengths, angles and areas. It also showed that isometric SfT is a well-posed problem. Other differential SfT methods that reconstruct non-isometric surfaces may use elasticity (Malti and Herzet, 2017; Malti et al., 2013) or smoothness (Bartoli and Özgür, 2016).

In this paper, we propose a novel and unified differential framework for SfT and NRSfM which encapsulates all properties of the surfaces and leads to simple deformation constraints derived only from the images. Recently, we presented a solution to isometric NRSfM (Parashar et al., 2017). Besides MT, it uses Christoffel Symbols (CS), which describe the local rate of change of MT. We showed that both CS and MT were transferable across surfaces using the image warps, the local non-parametric registration of images. Due to these transfer laws, the number of variables remains constant for any number of images. However, this solution cannot be extended to deformations other than isometry. This is because, unlike MT, CS can only be transferred for isometric deformations, as explained in appendix A. In this paper, we first study the extent of deformations modeled by MT and then propose solutions to SfT and NRSfM for all these deformation models. More specifically, we bring the following contributions.

1) Deformation modeling. We define an algebraic deformation model as a deformation model which can be formulated using a polynomial function of the components of MT. We consider the set of physically feasible deformations that correspond to low-order polynomials. Isometry and conformity are trivially in this set. We show that the well-known equiareal (area-preserving) deformations are also in this set. We introduce the skewless deformations which are inclusive of isometry and conformity and have an overlap with equiareality. Isometry, conformity, equiareality and skewlessness form the main set of algebraic deformation models.

2) Solving SfT. We use the theory of connections and moving frames developed by the French mathematician Cartan (Cartan, 1923, 1937). A moving frame is a local frame of reference defined at a point on the manifold. An MT is expressed uniquely in terms of its underlying moving frame. Cartan developed the theory of connections by defining the local transformation of the surface to its neighborhood whose components are the Cartan's Connections (CC). CC are derived using the moving frame and its derivatives. They are a compact representation of the first, second and third fundamental forms of surfaces. These forms describe the measurements, curvatures and orientation which encapsulate all characteristics of the surfaces in a compact way. CS form a subset of CC. We use the assumption of infinitesimal linearity (IL) which is widely used in differential geometry (Kock, 2010). It allows a smooth mapping between surfaces to be expressed as a set of linear mappings between infinitesimal portions of the surfaces. With IL, we show that CC are transferable across surfaces using the image warps. We also use the assumption of infinitesimal planarity (IP), proposed in (Chhatkuli et al., 2014), where surfaces are assumed to be infinitesimally planar while remaining curved. Using IP, we formulate and solve SfT for all algebraic deformation models using only the constraints from MT and its derivatives. With IP and IL, CC can be linearly transferred across the surfaces. Using the transfer laws of MT and CC, we formulate a generic solution to SfT which does not use MT-based deformation modeling and reconstructs both isometric and non-isometric surfaces. This leads to differential constraints which relate corresponding points on the surfaces under consideration. These constraints are local as they are defined for each point correspondence independently. We formulate all solutions in terms of Partial Differential Equations (PDEs). We convert the PDEs to algebraic equations and solve them locally.

3) Solving NRSfM. Using IP, IL and the transfer laws of MT and CC, we solve NRSfM for all algebraic deformation models except equiareality, which we show is unsolvable.

We compare the proposed methods with the state-of-the-art. Experiments show that our methods are generally more accurate. Since our solutions are obtained by solving simple polynomial equations, they are also much faster.

2 Previous Work

The 3D reconstruction of rigid objects is widely considered to be a theoretically solved problem due to the well-formulated projective framework of SfM. However, the 3D reconstruction of deformable objects still remains an open research problem due to the complexity of deformations and inability of current approaches to extend their proposed frameworks to a wider range of deformations. Even with the depth images available using Kinect or any other active sensor, for example (Innmann et al., 2016; Newcombe et al., 2015; Zollhöfer et al., 2018), one needs to refine the point cloud to obtain a geometrically consistent and temporally-coherent reconstruction of objects under consideration. In the best case scenario, most of these active sensors are easily off by centimeters. Some approaches replace them with a synchronized system of multiple cameras. They may reconstruct a 3D model, like in (Cagniart et al., 2010; Starck and Hilton, 2003), and track it through multiple views or obtain multiple spatial and temporally-coherent 3D surfaces as in (De Aguiar et al., 2008). These systems are huge and expensive and therefore, inapplicable in many scenarios such as medical endoscopy. Recently, learning-based single-view reconstruction methods (Mehta et al., 2018; Pumarola et al., 2018; Tewari et al., 2018; Zhou et al., 2018) have been proposed. They are object-specific and rely on training data which are very difficult to obtain.

Early approaches to deformable 3D reconstruction assume that the space of shapes under deformation is low dimensional. This led to the statistical models formulated using a low-rank constraint. (Bregler et al., 2000) used the low-rank shape-basis to solve NRSfM, (Del Bue et al., 2004) proposed a non-linear refinement to improve this solution by dealing with ambiguities. (Torresani et al., 2001) and (Olsen and Bartoli, 2008) used additional priors related to spatial and temporal smoothness. (Akhter et al., 2009) replaced the shape-basis with the trajectory-basis to

constrain deformations temporally. (Gotardo and Martinez, 2011) used a combination of shape and trajectory-basis, with a DCT-basis to model high deformations. Most of these methods require fixing the dimension of the shape-basis which may be a problem in case of large deformations. (Dai et al., 2014) proposed to automatically estimate it using a convex relaxation of the minimum rank condition and solved NRSfM using convex optimization. Statistics-based methods are well adapted to video sequences but they have difficulties handling complex deformations and missing data, which are generally overcome by physics-based methods.

While statistics-based methods obtain a global solution as they constrain all visible points of the object in all images, physics-based methods obtain a global, piece-wise or local solution. Mesh-based methods produce either global or piece-wise solutions. The global approaches using the isometric model include (Chhatkuli et al., 2017a) based on convex optimization and the Maximum Depth Heuristic (MDH) and (Vicente and Agapito, 2012) which imposes isometry using iterative optimization. Elastic mesh-based methods are also global as they require boundary conditions (Haouchine et al., 2014) or mixing the low-rank model with elastic material constraints (Agudo and Moreno-Noguer, 2015; Agudo et al., 2016). Piece-wise methods impose isometry (Taylor et al., 2010; Varol et al., 2009) or local rigidity (Russell et al., 2014). These methods require stitching all pieces together to recover the surface. Although mesh-based methods obtain decent results, they suffer from the inability to model the exact constraints, primarily isometry. Also the global and piece-wise solutions that these methods obtain are computationally expensive as they rely on a heavy refinement process. Differential methods formulate constraints locally at each point on the surface using differential properties of deformations. Their solutions are local except for elastic methods which require a global solution. In isometric SfT, differential methods obtain the surface's normals and depth locally (Bartoli et al., 2015; Chhatkuli et al., 2017b). These local solutions are often analytic, which means that they are obtained by solving simple algebraic equations, making them very fast. Local solutions can be further improved using non-linear refinement methods such as (Brunet et al., 2014). In isometric SfT, the refinement process is quite fast and close to the local analytic solution (Chhatkuli et al., 2017b). Other differential methods explore non-isometric models such as the conformal model (Bartoli et al., 2015) or (Bartoli and Özgür, 2016) where normals are locally recovered by imposing only smoothness and local planarity. The latter is however not a stable method, requiring significant perspective in the images to yield a good reconstruction. Refinement is also used to improve the solution. Global differential methods, elastic SfT (Malti and Herzet, 2017; Malti et al., 2013) for example, use differential constraints but the surface is obtained globally using variational methods that exploit boundary conditions. The differential modeling is rather new to NRSfM as compared to SfT. (Chhatkuli et al., 2014) models isometry as local rigidity of infinitesimal planes and (Parashar et al., 2017) models the exact isometric constraint using MT and exploits CS constraints to obtain a local, analytical solution.

We extend the differential modeling of (Bartoli et al., 2015) and propose deformable 3D reconstruction algorithms. Our main contributions are: *1)* We define and derive the complete set of possible algebraic deformation models related to isotropic (isometric and conformal), orthotropic (skewless) and anisotropic (equiareal) deformations. *2)* We propose the MT-CC framework, which replaces the MT-CS framework of our previously proposed isometric NRSfM (Parashar et al., 2017) and use it to solve SfT and NRSfM. *3)* Under MT-CC, SfT can be solved for all deformation models by using MT constraints or a generic solution can be formed by using CC only. All proposed SfT methods except skewless SfT are linear. *4)* Under MT-CC, NRSfM can be solved for all but equiareal deformations under the assumption of IP and IL. We show that due to their isotropic nature, isometric and conformal NRSfM possess a joint solution. We show that equiareal NRSfM is not solvable. *5)* Not only MT-CC derives existing results (Bartoli et al., 2015; Parashar et al., 2017) in a much simpler way but also unifies the formulation of SfT and NRSfM. Both are represented by the same reconstruction equations but SfT has fewer variables than NRSfM. *6)* Our proposed SfT and NRSfM methods are local solutions; they are extremely fast and handle missing data naturally.

3 Mathematical Background

We model the surfaces as smooth manifoldsand the cameras as perspective projection. The image embedding is expressed as in (Parashar et al., 2017). More details can be found in appendix B. We now describe CC, moving frames and their relationships. We then review the deformation models, IP and IL.

Notation. We use small-case Latin letters to denote scalars and small-case Greek letters to denote functions. Bold and small Latin letters denote 2D and 3D vectors. We use a subscript to index the images and a superscript to index the coordinates of a point. d represents total differentiation. $|.|$ represents the determinant. We use $\mathbf{J}$ to write the jacobians. The coordinate basis vectors at a point in n-dimensional space are given by $\mathbf{e}_i$ where $i \in [1, ..., n]$. Differential 1-forms (Cartan, 1970) are denoted as w. The origin is denoted as $\mathbf{O}$. In order to make the equations compact, we omit the point $\mathbf{x}$ while expressing functions. For example, $\beta_i(\mathbf{x})$ and $\phi_i(\mathbf{x})$ on the i^{th} image are written as β_i and ϕ_i. We also write $\frac{\partial \beta_i}{\partial x^t}$ as β_{it}, $\frac{\partial \phi_i}{\partial x^t}$ as ϕ_{it}, $\frac{\partial^2 \phi_i}{\partial x^t \partial x^s}$ as ϕ_{its} and $\frac{\partial^2 \beta_i}{\partial x^t \partial x^s}$ as β_{its}.

3.1 Cartan's Connections

In differential geometry, a connection is defined as a geometric object attached to a point on a smooth manifold.

Definition 1. *Cartan's connection is a set of geometric relations expressed in terms of the affine moving frame defined locally at a point in space that relate a point to its infinitesimal neighborhood.*

We use the affine connection described by Cartan (Cartan, 1923). In order to define such a connection in an n-dimensional space, we fix an origin $\mathbf{O}$ and n linearly independent basis vectors $(\mathbf{e}_1, \mathbf{e}_2, \ldots, \mathbf{e}_n)$ originating from $\mathbf{O}$ which describe a frame at point $\mathbf{z}$ on the manifold as:

$$\mathbf{z} = \mathbf{O} + z^1\mathbf{e}_1 + z^2\mathbf{e}_2 + ... + z^n\mathbf{e}_n, \tag{1}$$

where z^t are the coordinates of $\mathbf{z}$. An affine connection is described using the 1-forms w^t and w_t^s known as *dual* and *connection* forms respectively. We explain them in appendix C. An affine connection is given by:

$$\begin{aligned} \mathrm{d}\mathbf{z} &= w^1\mathbf{e}_1 + w^2\mathbf{e}_2 + \ldots + w^n\mathbf{e}_n \\ \mathrm{d}\mathbf{e}_t &= w_t^1\mathbf{e}_1 + w_t^2\mathbf{e}_2 + \ldots + w_t^n\mathbf{e}_n, \end{aligned} \tag{2}$$

A connection 1-form describes the change in the moving frame as one moves to the infinitesimal neighborhood of a point on the manifold. An affine connection defines the local geometric and physical properties (such as unit lengths and areas) of the affine space around a point in the manifold. Cartan's vision behind connections (Cartan, 1923, 1924, 1926) was to define geometric properties on an object without physically defining the object. He derived these laws using the theory of moving frames (Cartan, 1937) which we now describe.

3.2 Moving Frames on Surfaces

A moving frame at a 3D surface $\mathcal{M}$ is a set of 3 linearly independent vectors. It can be defined in several ways. The connection forms defined in equation (2) are dependent on the moving frame. In general we assume that any point

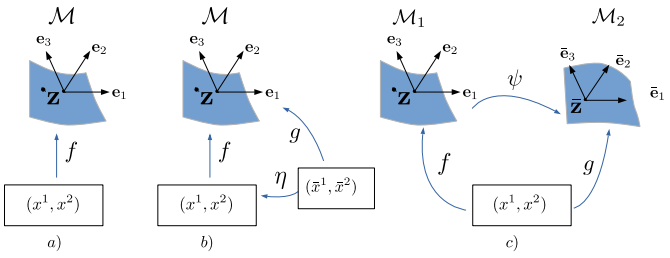

Fig. 1: a) A moving frame on a surface $\mathcal{M}$ defined using a local parametrization (x^1, x^2). b) A moving frame on a surface $\mathcal{M}$ defined using local parametrizations (x^1, x^2) and $(\bar{x}^1, \bar{x}^2)$ related by η. c) Two surfaces $\mathcal{M}_1$ and $\mathcal{M}_2$ related by ψ are parametrized using (x^1, x^2).

on the surface manifold admits a local parametrization described by the function $f(x^1, x^2)$, see figure 1a. A natural choice is to use tangent vectors of the surface to define a moving frame:

$$\mathbf{e}_1 = \frac{\partial f}{\partial x^1} \qquad \mathbf{e}_2 = \frac{\partial f}{\partial x^2} \qquad \mathbf{e}_3 = \frac{\partial f}{\partial x^1} \times \frac{\partial f}{\partial x^2}, \tag{3}$$

with $\mathbf{e}_1^\top \mathbf{e}_3 = 0$ and $\mathbf{e}_2^\top \mathbf{e}_3 = 0$. The expression of the total derivative at $\mathbf{z}$ in terms of the moving frame is given by:

$$\mathrm{d}\mathbf{z} = \frac{\partial f}{\partial x^1}\mathrm{d}x^1 + \frac{\partial f}{\partial x^2}\mathrm{d}x^2. \tag{4}$$

By identifying the terms in equation (4) with equation (2), one obtains the dual forms $w^1 = \mathrm{d}x^1$, $w^2 = \mathrm{d}x^2$ and $w^3 = 0$. The connection forms can be found by taking the total derivative of the basis vectors:

$$\mathrm{d}\mathbf{e}_t = \frac{\partial \mathbf{e}_t}{\partial x^1}\mathrm{d}x^1 + \frac{\partial \mathbf{e}_t}{\partial x^2}\mathrm{d}x^2, \tag{5}$$

and finding the representation of equation (5) in the basis formed by the moving frame $(\mathbf{e}_1, \mathbf{e}_2, \mathbf{e}_3)$:

$$\mathrm{d}\mathbf{e}_t = w_t^1\mathbf{e}_1 + w_t^2\mathbf{e}_2 + w_t^3\mathbf{e}_3, \tag{6}$$

where $w_t^s = \Gamma_{t1}^s \mathrm{d}x^1 + \Gamma_{t2}^s \mathrm{d}x^2$ and Γ_{tk}^s are scalar functions. Given the frame in equation (3), Γ_{tk}^s for $s, t, k \in \{1, 2\}$ are its CS and Γ_{tk}^s with $s = 3$ and $t, k \in \{1, 2\}$ are the second fundamental form.

Example 1. *Given the following surface of a plane:*

$$f(x^1, x^2) = \mathbf{u}x^1 + \mathbf{v}x^2 + \mathbf{o}, \tag{7}$$

where $\mathbf{u}$ *and* $\mathbf{v}$ *are three-dimensional unit vectors that define the plane and* $\mathbf{o}$ *is a three-dimensional displacement vector, we have the moving frame of equation* (3) *as:*

$$\mathbf{e}_1 = \mathbf{u} \quad \mathbf{e}_2 = \mathbf{v} \quad \mathbf{e}_3 = \mathbf{u} \times \mathbf{v}. \tag{8}$$

The total derivative is given by:

$$\mathrm{d}\mathbf{z} = \begin{pmatrix} \mathrm{d}x^1 & \mathrm{d}x^2 \end{pmatrix} \begin{pmatrix} \mathbf{u} & \mathbf{v} \end{pmatrix}^\top = \begin{pmatrix} \omega^1 & \omega^2 \end{pmatrix} \begin{pmatrix} \mathbf{e}_1 & \mathbf{e}_2 \end{pmatrix}^\top. \tag{9}$$

As $\mathbf{e}_1$ *and* $\mathbf{e}_2$ *are constant vectors then* $\mathrm{d}\mathbf{e}_1 = 0$ *and* $\mathrm{d}\mathbf{e}_2 = 0$. *This makes all connection forms* $w_t^s = 0$ *for* $t \in \{1, 2\}$ *and* $s \in \{1, 2, 3\}$. *This result holds for the particular parametrization of the plane* (7) *and the moving frame* (8).

Example 2. *If the plane* (7) *is projected into the image with coordinates* $(\bar{x}_1, \bar{x}_2)$, *it can be alternatively parametrized using the image embedding* ϕ *as:*

$$\phi = \frac{1}{\beta(\bar{x}^1, \bar{x}^2)} \begin{pmatrix} \bar{x}^1 \\ \bar{x}^2 \\ 1 \end{pmatrix}, \tag{10}$$

with:

$$\beta(\bar{x}^1, \bar{x}^2) = -\frac{\mathbf{n}^\top \begin{pmatrix} \bar{x}^1 & \bar{x}^2 & 1 \end{pmatrix}^\top}{\mathbf{n}^\top \mathbf{o}} \qquad \mathbf{n} = \mathbf{u} \times \mathbf{v}. \tag{11}$$

The moving frame on the surface $\mathcal{M}$ *described by the image embedding* (11) *is given by:*

$$\begin{aligned} \mathbf{e}_1 = \phi_1 &= \left(\frac{1}{\beta}\right)^2 \begin{pmatrix} \beta - \bar{x}^1\beta_1, -\bar{x}^2\beta_1, -\beta_1 \end{pmatrix}^\top \\ \mathbf{e}_2 = \phi_2 &= \left(\frac{1}{\beta}\right)^2 \begin{pmatrix} -\bar{x}^1\beta_2, \beta - \bar{x}^2\beta_2, -\beta_2 \end{pmatrix}^\top \\ \mathbf{e}_3 = \phi_1 \times \phi_2 &= \left(\frac{1}{\beta}\right)^3 \begin{pmatrix} \beta_1, \beta_2, \beta - \bar{x}^1\beta_1 - \bar{x}^2\beta_2 \end{pmatrix}^\top, \end{aligned} \tag{12}$$

where $(\beta_1, \beta_2) = \left(\frac{\partial \beta}{\partial \bar{x}^1}, \frac{\partial \beta}{\partial \bar{x}^2}\right)$. *Using the frame and its first-order derivatives, we obtain the connection forms* w_t^s *for* ϕ. *We write* $w_t^s = \Gamma_{tk}^s \mathrm{d}\bar{x}^k$ *and obtain:*

$$\begin{aligned} \begin{pmatrix} \Gamma_{11}^1 & \Gamma_{11}^2 & \Gamma_{11}^3 \\ \Gamma_{21}^1 & \Gamma_{21}^2 & \Gamma_{21}^3 \\ \Gamma_{31}^1 & \Gamma_{31}^2 & \Gamma_{31}^3 \end{pmatrix} &= -\frac{1}{\beta} \begin{pmatrix} 2\beta_1 & 0 & 0 \\ \beta_2 & \beta_1 & 0 \\ 0 & 0 & 3\beta_1 \end{pmatrix} \\ \begin{pmatrix} \Gamma_{12}^1 & \Gamma_{12}^2 & \Gamma_{12}^3 \\ \Gamma_{22}^1 & \Gamma_{22}^2 & \Gamma_{22}^3 \\ \Gamma_{32}^1 & \Gamma_{32}^2 & \Gamma_{32}^3 \end{pmatrix} &= -\frac{1}{\beta} \begin{pmatrix} \beta_2 & \beta_1 & 0 \\ 0 & 2\beta_2 & 0 \\ 0 & 0 & 3\beta_2 \end{pmatrix}. \end{aligned} \tag{13}$$

As expected, the connections in examples 1 and 2 are different. Equation (13) plays an important role as it shows the general structure of the connection's coefficients derived using image embeddings for planar surfaces. Using IP, these coefficients are extended to non-planar surfaces.

3.3 Moving Frames and Surface Parametrizations

Figure 1b shows a surface $\mathcal{M}$ defined using two different parametrizations $f(\mathbf{x})$ and $g(\bar{\mathbf{x}})$. The domains of f and g are mutually homeomorphic and η is the diffeomorphic mapping that expresses the change of coordinates:

$$\mathbf{x} = \eta(\bar{\mathbf{x}}) = \begin{pmatrix} \eta^1(\bar{\mathbf{x}}) \\ \eta^2(\bar{\mathbf{x}}) \end{pmatrix}. \tag{14}$$

By differentiation, we obtain the relationship between the dual forms of the two parametrizations as:

$$\mathrm{d}x^1 = \frac{\partial x^1}{\partial \bar{x}^1}\mathrm{d}\bar{x}^1 + \frac{\partial x^1}{\partial \bar{x}^2}\mathrm{d}\bar{x}^2 \quad \mathrm{d}x^2 = \frac{\partial x^2}{\partial \bar{x}^1}\mathrm{d}\bar{x}^1 + \frac{\partial x^2}{\partial \bar{x}^2}\mathrm{d}\bar{x}^2. \tag{15}$$

Given that $g = f \circ \eta$ in figure 1b, we obtain $\mathbf{J}_g = \mathbf{J}_f\mathbf{J}_\eta$. Therefore, the moving frames vectors $(\bar{\mathbf{e}}_1, \bar{\mathbf{e}}_2, \bar{\mathbf{e}}_3)$ and $(\mathbf{e}_1, \mathbf{e}_2, \mathbf{e}_3)$ defined using $(\bar{x}^1, \bar{x}^2)$ and (x^1, x^2) respectively are related by the following relationship:

$$\begin{aligned} \begin{pmatrix} \bar{\mathbf{e}}_1 & \bar{\mathbf{e}}_2 \end{pmatrix} &= \begin{pmatrix} \mathbf{e}_1 & \mathbf{e}_2 \end{pmatrix} \mathbf{J}_\eta \\ \bar{\mathbf{e}}_3 = \bar{\mathbf{e}}_1 \times \bar{\mathbf{e}}_2 &= |\mathbf{J}_\eta|(\mathbf{e}_1 \times \mathbf{e}_2) = |\mathbf{J}_\eta|\mathbf{e}_3 \\ \begin{pmatrix} \bar{\mathbf{e}}_1 & \bar{\mathbf{e}}_2 & \bar{\mathbf{e}}_3 \end{pmatrix} &= \begin{pmatrix} \begin{pmatrix} \mathbf{e}_1 & \mathbf{e}_2 \end{pmatrix} \mathbf{J}_\eta & |\mathbf{J}_\eta|\mathbf{e}_3 \end{pmatrix} \\ &= \begin{pmatrix} \mathbf{e}_1 & \mathbf{e}_2 & \mathbf{e}_3 \end{pmatrix} \mathrm{diag}(\mathbf{J}_\eta, |\mathbf{J}_\eta|). \end{aligned} \tag{16}$$

Differentiating the above relation and expressing the derivatives of frame bases according to equation (2), we obtain:

$$\begin{aligned} \begin{pmatrix} \bar{\mathbf{e}}_1^\top \\ \bar{\mathbf{e}}_2^\top \\ \bar{\mathbf{e}}_3^\top \end{pmatrix}^\top \begin{pmatrix} \bar{w}_1^1 & \bar{w}_2^1 & \bar{w}_3^1 \\ \bar{w}_1^2 & \bar{w}_2^2 & \bar{w}_3^2 \\ \bar{w}_1^3 & \bar{w}_2^3 & \bar{w}_3^3 \end{pmatrix} &= \begin{pmatrix} \mathbf{e}_1^\top \\ \mathbf{e}_2^\top \\ \mathbf{e}_3^\top \end{pmatrix}^\top \mathrm{diag}(\mathrm{d}\mathbf{J}_\eta, \mathrm{d}|\mathbf{J}_\eta|) \\ &+ \begin{pmatrix} \mathbf{e}_1^\top \\ \mathbf{e}_2^\top \\ \mathbf{e}_3^\top \end{pmatrix}^\top \begin{pmatrix} w_1^1 & w_2^1 & w_3^1 \\ w_1^2 & w_2^2 & w_3^2 \\ w_1^3 & w_2^3 & w_3^3 \end{pmatrix} \mathrm{diag}(\mathbf{J}_\eta, |\mathbf{J}_\eta|). \end{aligned} \tag{17}$$

Substituing equation (16) in the equation (17), we write the relation between connection forms as:

$$\begin{aligned} \begin{pmatrix} \bar{w}_1^1 & \bar{w}_2^1 & \bar{w}_3^1 \\ \bar{w}_1^2 & \bar{w}_2^2 & \bar{w}_3^2 \\ \bar{w}_1^3 & \bar{w}_2^3 & \bar{w}_3^3 \end{pmatrix} &= \mathrm{diag}(\mathbf{J}_\eta^{-1}, |\mathbf{J}_\eta|^{-1})\mathrm{diag}(\mathrm{d}\mathbf{J}_\eta, \mathrm{d}|\mathbf{J}_\eta|) \\ &+ \mathrm{diag}(\mathbf{J}_\eta^{-1}, |\mathbf{J}_\eta|^{-1}) \begin{pmatrix} w_1^1 & w_2^1 & w_3^1 \\ w_1^2 & w_2^2 & w_3^2 \\ w_1^3 & w_2^3 & w_3^3 \end{pmatrix} \mathrm{diag}(\mathbf{J}_\eta, |\mathbf{J}_\eta|). \end{aligned} \tag{18}$$

Equations (16) and (18) show that the moving frame and connections of the 3D surface $\mathcal{M}$ (in figure 1b) derived using the functions f and g are linearly related in terms of the first and second-order derivatives of η. We refer to these equations as the change of variable equations of moving frames and connections. In the next section, we show how to draw relationships between different surfaces.

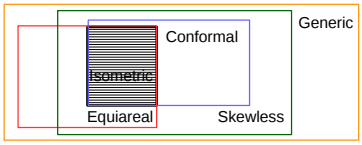

Fig. 2: Classification of algebraic deformation models. Isometry is well-constrained and widely studied. It is a combination of conformity and equiareality.

3.4 Mappings between Surfaces

Mappings are defined by functions that connect points between two surfaces. Figure 1c shows a mapping $\psi : \mathcal{M}_1 \to \mathcal{M}_2$ between surfaces $\mathcal{M}_1$ and $\mathcal{M}_2$, respectively parametrized by embeddings f and g. The mapping ψ takes a point $\mathbf{z}$ on $\mathcal{M}_1$ and transports it to $\bar{\mathbf{z}}$ on $\mathcal{M}_2$. Therefore, $\bar{\mathbf{z}} = \psi(\mathbf{z})$. We assume that mappings between surfaces are diffeomorphic, which implies that they are smooth, bijective and with a smooth inverse.

Algebraic deformation models. Surface mappings are associated with surface deformations; therefore, they identify with a deformation model. We study the set of mappings whose deformation model can be expressed in terms of the surface metric properties such as lengths, angles and areas defined using MT. We define an algebraic deformation model as a set of constraints that preserve some metric quantities across surfaces formulated using a polynomial function of the components of MT. Although it is possible to construct several polynomials using MT, not all of them may represent a physical deformation. Also the higher order polynomials, even though they may possibly represent a physical deformation, dramatically increase the solution complexity. Therefore, we restrict ourselves to the set of low-order polynomials that correspond to physically feasible deformation models. Figure 2 categorizes the surface mappings according to the metric quantities they preserve: *1)* isometric (distances-preserving), *2)* conformal (angle-preserving), *3)* equiareal (area-preserving) and *4)* skewless (orthogonal frame basis' angle-preserving). The set of isometric mappings is a subset of 2), 3) and 4) and is also given by the intersection of 2) and 3). The set of skewless mappings includes 1), 2) and a subset of 3).

Mathematical formulation. The metric quantities on surfaces can be expressed locally in terms of moving frames, therefore deformation models are expressed in terms of the first-order differential constraints. (Bartoli et al., 2015; Parashar et al., 2017) proposed to formulate deformations using MT, which can then be expressed in terms of moving frames. Appendix D discusses this relation.

Given the moving frames $(\mathbf{e}_1, \mathbf{e}_2, \mathbf{e}_3)$ at $\mathcal{M}_1$ and $(\bar{\mathbf{e}}_1, \bar{\mathbf{e}}_2, \bar{\mathbf{e}}_3)$ at $\mathcal{M}_2$ from equation (3), we discuss the formulation of deformation models for the mappings in figure 2.

1) Isometric mappings. They preserve lengths and angles of the moving frames at the corresponding points on the two surfaces. The constraints are:

$$\bar{\mathbf{e}}_1^\top \bar{\mathbf{e}}_1 = \mathbf{e}_1^\top \mathbf{e}_1 \qquad \bar{\mathbf{e}}_2^\top \bar{\mathbf{e}}_2 = \mathbf{e}_2^\top \mathbf{e}_2 \qquad \bar{\mathbf{e}}_1^\top \bar{\mathbf{e}}_2 = \mathbf{e}_1^\top \mathbf{e}_2. \tag{19}$$

2) Conformal mappings. They preserve angles of the moving frames at the corresponding points on the two surfaces but the frame vectors are isotropically rescaled. The constraints are:

$$\begin{pmatrix} \bar{\mathbf{e}}_1^\top \bar{\mathbf{e}}_1 & \bar{\mathbf{e}}_2^\top \bar{\mathbf{e}}_2 & \bar{\mathbf{e}}_1^\top \bar{\mathbf{e}}_2 \end{pmatrix} \propto \begin{pmatrix} \mathbf{e}_1^\top \mathbf{e}_1 & \mathbf{e}_2^\top \mathbf{e}_2 & \mathbf{e}_1^\top \mathbf{e}_2 \end{pmatrix}. \tag{20}$$

3) Equiareal mappings. They preserve area, expressed as the squared norm of the cross product of the tangent vectors at the corresponding points on the two surfaces:

$$\|\bar{\mathbf{e}}_1 \times \bar{\mathbf{e}}_2\|^2 = \|\mathbf{e}_1 \times \mathbf{e}_2\|^2. \tag{21}$$

4) Skewless mappings. They preserve angles along the orthogonal frame basis on the surface. A skewless mapping is

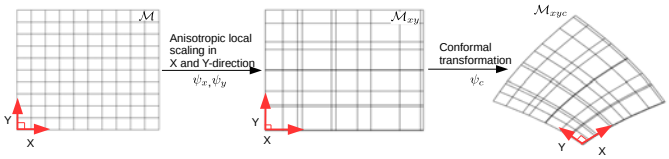

Fig. 3: An example of skewless deformation. A surface grid undergoes anisotropic scaling in two orthogonal directions and then undergoes a conformal transformation. Therefore, only the angles between the basis vectors are preserved.

composed of local orthotropic scalings along the frame basis followed by a conformal mapping, as shown in figure 3. This decomposition is unique up to a scale factor. Theorem 1 formalises the construction of these mappings and the proof can be found in appendix E.

Theorem 1 (Skewless mappings). *A mapping is skewless iff it can be decomposed into a conformal mapping and orthotropic scalings along the orthogonal frame basis.*

The constraint for skewless mappings is:

$$\frac{\left(\bar{\mathbf{e}}_1^\top \bar{\mathbf{e}}_2\right)^2}{\left(\bar{\mathbf{e}}_1^\top \bar{\mathbf{e}}_1\right)\left(\bar{\mathbf{e}}_2^\top \bar{\mathbf{e}}_2\right)} = \frac{\left(\mathbf{e}_1^\top \mathbf{e}_2\right)^2}{\left(\mathbf{e}_1^\top \mathbf{e}_1\right)\left(\mathbf{e}_2^\top \mathbf{e}_2\right)}. \tag{22}$$

In sections 4 and 5, we show how to exploit these properties expressed in terms of moving frames for 3D reconstruction.

3.5 Infinitesimal Planarity

Under the assumption of IP, a surface is approximated to be planar in its infinitesimal neighborhood while maintaining its curvature globally. Therefore at an infinitesimal level, the surface matches its tangent plane. This allows the surface to be point-wise planar. As a consequence, β in equation (10) becomes a linear function. Therefore, the connection's coefficients on the surface can be expressed using equation (13).

Isometric mappings have a special property which we present in the following theorem proved in appendix E.

Theorem 2 (Isometric mappings). *An isometric mapping between two planes preserves the connection forms* $(w_1^1, w_2^1, w_1^2, w_2^2)$.

Using IP, we extend theorem 2 to non-planar surfaces in the next corollary.

Corollary 1 (Isometric mappings under IP). *Under IP, an isometric mapping between two non-planar surfaces preserves the connection forms* $(w_1^1, w_2^1, w_1^2, w_2^2)$.

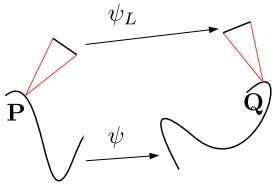

Fig. 4: Illustration of IL. Two smooth curves are related by a mapping ψ. According to IL, there exists a linear map ψ_L that relates $\mathbf{P}$ and $\mathbf{Q}$ and agrees with ψ at zeroth and first-order.

3.6 Infinitesimal Linearity

IL assumes that a smooth mapping between two surfaces can be represented by a set of linear mappings which map the infinitesimal neighborhoods of the corresponding points on surfaces. Figure 4 shows two curves related by a smooth mapping ψ. According to the formulation of IL in synthetic differential geometry (Kock, 2010), given that ψ maps $\mathbf{P}$ to $\mathbf{Q}$, there exists at least one linear function ψ_L that maps the infinitesimal neighborhood of $\mathbf{P}$ to $\mathbf{Q}$. Thus, ψ is represented with an infinite set of linear mappings ψ_L that map infinitesimal neighborhoods of the curves $\mathbf{P}$ and $\mathbf{Q}$. ψ_L has the same first-order differentials as ψ. It only assumes that the second and higher-order differentials are zero as it is a linearization of ψ. Theorem 3, proved in appendix E, states an important property of linear mappings.

Theorem 3 (Linear mappings). *A linear mapping between two planes preserves the connection forms* $(w_1^1, w_2^1, w_1^2, w_2^2)$.

For IL mappings, we extend theorem 3 to non-planar surfaces in the next corollary.

Corollary 2 (Infinitesimally linear mappings). *An IL mapping between two surfaces preserves the connection forms* $(w_1^1, w_2^1, w_1^2, w_2^2)$.

We always use IP and use IL in specific cases to formulate the reconstruction algorithms in sections 4 and 5.

4 Template-Based Deformable 3D Reconstruction

We use our MT-CC framework to model and solve template-based deformable 3D reconstruction, also known as SfT. We present two approaches: 1) modeling deformations shown in figure 2 by using constraints on moving frames under IP and 2) using geometric properties of connections under IP and IL, thus avoiding the deformation modeling of section 3. Our solutions are obtained by solving a system of polynomials. We discuss the well-posedness (uniqueness) of our solutions. (Chhatkuli et al., 2017b) proved that the isometric SfT solution to depth is non-stable in affine conditions, which means that depth is not constrained when the projection becomes affine. Hence, it is not always possible to solve for depth. We solve for depth-derivatives which lead to surface normals. We discuss the stability of normals obtained from our methods which are found to be stable for the isometric SfT in (Chhatkuli et al., 2017b).

4.1 General Model

Figure 5 shows the general model. Given a 3D template $\mathcal{T}$ of the object, our goal is to find the surface $\mathcal{M}$ as observed in image $\mathcal{I}$. η is the image warp from $\mathcal{I}$ to the flattened 3D template $\mathcal{P}$. η is known and can be estimated in practice with dense image registration methods. ψ is the deformation mapping between $\mathcal{T}$ and $\mathcal{M}$. For rigid objects ψ is a Euclidean transformation. We model the template $\mathcal{T}$ and the surface $\mathcal{M}$ using image embeddings ϕ_1 and ϕ_2:

$$\phi_1(x^1, x^2) = \frac{1}{\beta_1(x^1, x^2)} \begin{pmatrix} x^1 \\ x^2 \\ 1 \end{pmatrix} \quad \phi_2(\bar{x}^1, \bar{x}^2) = \frac{1}{\beta_2(\bar{x}^1, \bar{x}^2)} \begin{pmatrix} \bar{x}^1 \\ \bar{x}^2 \\ 1 \end{pmatrix}. \tag{23}$$

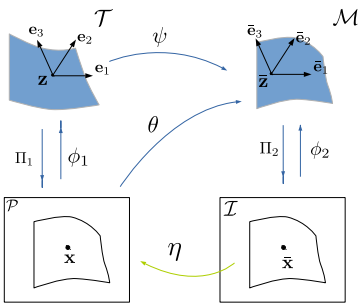

Fig. 5: Modeling of template-based 3D reconstruction of deformable objects from a single view.

The moving frames $(\mathbf{e}_1^t, \mathbf{e}_2^t, \mathbf{e}_3^t)$ and $(\bar{\mathbf{e}}_1, \bar{\mathbf{e}}_2, \bar{\mathbf{e}}_3)$ on $\mathcal{T}$ and $\mathcal{M}$ respectively are derived using equation (12). We write the following expressions from the moving frames on $\mathcal{T}$:

$$\begin{aligned}
\left(\mathbf{e}_1^t\right)^\top \mathbf{e}_1^t &= \frac{1}{k^2}\left(\epsilon^2 k_1^2 + 1 - 2x^1 k_1\right) = \frac{E_t}{k^2} \\
\left(\mathbf{e}_2^t\right)^\top \mathbf{e}_2^t &= \frac{1}{k^2}\left(\epsilon^2 k_2^2 + 1 - 2x^2 k_2\right) = \frac{G_t}{k^2} \\
\left(\mathbf{e}_1^t\right)^\top \mathbf{e}_2^t &= \frac{1}{k^2}\left(\epsilon^2 k_1 k_2 - x^1 k_2 - x^2 k_1\right) = \frac{F_t}{k^2},
\end{aligned} \tag{24}$$

where $\epsilon^2 = \left(1 + \left(x^1\right)^2 + \left(x^2\right)^2\right)$, $k = \beta_1$, $k_1 = \dfrac{\beta_{11}}{\beta_1}$ and $k_2 = \dfrac{\beta_{12}}{\beta_1}$. Under IP, the first-order derivatives of these expressions are given by:

$$\begin{aligned}
\frac{\partial E_t}{\partial x^1} &= -2k_1 E_t \quad \frac{\partial F_t}{\partial x^1} = -k_2 E_t - k_1 F_t \quad \frac{\partial G_t}{\partial x^1} = -2k_2 F_t \\
\frac{\partial E_t}{\partial x^2} &= -2k_1 F_t \quad \frac{\partial F_t}{\partial x^2} = -k_1 G_t - k_2 F_t \quad \frac{\partial G_t}{\partial x^2} = -2k_2 G_t.
\end{aligned} \tag{25}$$

Similarly, we can write $(\bar{E}, \bar{F}, \bar{G})$ and their first-order derivatives for $(\bar{\mathbf{e}}_1, \bar{\mathbf{e}}_2, \bar{\mathbf{e}}_3)$ at $\mathcal{M}$ in terms of $(\bar{k}_1, \bar{k}_2, \bar{k})$. In order to compare the moving frames at surfaces $\mathcal{T}$ and $\mathcal{M}$, we need to define them in the same parametrization space. Therefore, we derive (E, F, G) at $\mathcal{M}$ in terms of $(\bar{x}^1, \bar{x}^2)$ using the change of variable of equation (16):

$$\begin{aligned}
E &= \left(\frac{\partial x^1}{\partial \bar{x}^1}\right)^2 E_t + 2\frac{\partial x^1}{\partial \bar{x}^1}\frac{\partial x^2}{\partial \bar{x}^1} F_t + \left(\frac{\partial x^2}{\partial \bar{x}^1}\right)^2 G_t \\
F &= \frac{\partial x^1}{\partial \bar{x}^1}\frac{\partial x^1}{\partial \bar{x}^2} E_t + \left(\frac{\partial x^1}{\partial \bar{x}^1}\frac{\partial x^2}{\partial \bar{x}^2} + \frac{\partial x^2}{\partial \bar{x}^1}\frac{\partial x^1}{\partial \bar{x}^2}\right) F_t + \left(\frac{\partial x^2}{\partial \bar{x}^1}\right)^2 G_t \\
G &= \left(\frac{\partial x^1}{\partial \bar{x}^2}\right)^2 E_t + 2\frac{\partial x^1}{\partial \bar{x}^2}\frac{\partial x^2}{\partial \bar{x}^2} F_t + \left(\frac{\partial x^2}{\partial \bar{x}^2}\right)^2 G_t.
\end{aligned} \tag{26}$$

The derivatives of (E, F, G) according to equation (25) are:

$$\begin{aligned}
\frac{\partial E}{\partial \bar{x}^1} &= -2\left(\frac{\partial x^1}{\partial \bar{x}^1}k_1 + \frac{\partial x^2}{\partial \bar{x}^1}k_2\right) E + 2\frac{\partial^2 x^1}{\partial\left(\bar{x}^1\right)^2} A + 2\frac{\partial x^2}{\partial\left(\bar{x}^1\right)^2} B \\
\frac{\partial E}{\partial \bar{x}^2} &= -2\left(\frac{\partial x^1}{\partial \bar{x}^1}k_1 + \frac{\partial x^2}{\partial \bar{x}^1}k_2\right) F + 2\frac{\partial^2 x^1}{\partial \bar{x}^1 \partial \bar{x}^2} A + 2\frac{\partial x^2}{\partial \bar{x}^1 \partial \bar{x}^2} B \\
\frac{\partial G}{\partial \bar{x}^1} &= -2\left(\frac{\partial x^1}{\partial \bar{x}^2}k_1 + \frac{\partial x^2}{\partial \bar{x}^2}k_2\right) F + 2\frac{\partial^2 x^1}{\partial \bar{x}^1 \partial \bar{x}^2} C + 2\frac{\partial x^2}{\partial \bar{x}^1 \partial \bar{x}^2} D \\
\frac{\partial G}{\partial \bar{x}^2} &= -2\left(\frac{\partial x^1}{\partial \bar{x}^2}k_1 + \frac{\partial x^2}{\partial \bar{x}^2}k_2\right) G + 2\frac{\partial^2 x^1}{\partial\left(\bar{x}^2\right)^2} C + 2\frac{\partial x^2}{\partial\left(\bar{x}^2\right)^2} D \\
\frac{\partial F}{\partial \bar{x}^1} &= -\left(\frac{\partial x^1}{\partial \bar{x}^1}k_1 + \frac{\partial x^2}{\partial \bar{x}^1}k_2\right) F - \left(\frac{\partial x^1}{\partial \bar{x}^2}k_1 + \frac{\partial x^2}{\partial \bar{x}^2}k_2\right) E \\
&\quad + \frac{\partial^2 x^1}{\partial \bar{x}^1 \partial \bar{x}^2} A + \frac{\partial x^2}{\partial \bar{x}^1 \partial \bar{x}^2} B + \frac{\partial^2 x^1}{\partial\left(\bar{x}^1\right)^2} C + \frac{\partial x^2}{\partial\left(\bar{x}^1\right)^2} D \\
\frac{\partial F}{\partial \bar{x}^2} &= -\left(\frac{\partial x^1}{\partial \bar{x}^1}k_1 + \frac{\partial x^2}{\partial \bar{x}^1}k_2\right) G - \left(\frac{\partial x^1}{\partial \bar{x}^2}k_1 + \frac{\partial x^2}{\partial \bar{x}^2}k_2\right) F \\
&\quad + \frac{\partial^2 x^1}{\partial \bar{x}^1 \partial \bar{x}^2} C + \frac{\partial x^2}{\partial \bar{x}^1 \partial \bar{x}^2} D + \frac{\partial^2 x^1}{\partial\left(\bar{x}^2\right)^2} A + \frac{\partial x^2}{\partial\left(\bar{x}^2\right)^2} B
\end{aligned} \tag{27}$$

where:

$$\begin{aligned}
A &= \frac{\partial x^1}{\partial \bar{x}^1}E_t + \frac{\partial x^2}{\partial \bar{x}^1}F_t,\ B = \frac{\partial x^1}{\partial \bar{x}^1}F_t + \frac{\partial x^2}{\partial \bar{x}^1}G_t \\
C &= \frac{\partial x^1}{\partial \bar{x}^2}E_t + \frac{\partial x^2}{\partial \bar{x}^2}F_t,\ D = \frac{\partial x^1}{\partial \bar{x}^2}F_t + \frac{\partial x^2}{\partial \bar{x}^2}G_t.
\end{aligned} \tag{28}$$

Now we have both (E, F, G) and $(\bar{E}, \bar{F}, \bar{G})$ with respect to the same parametrization space $(\bar{x}_1, \bar{x}_2)$. We discuss next the solutions based on moving frames and connections.

4.2 Solutions using Deformation Modeling

We derive constraints for the deformation models of equations (19)-(22), which are formulated using moving frames only. We use IP to derive these constraints. Since (k_1, k_2, k) are known, our goal is to find $(\bar{k}_1, \bar{k}_2, \bar{k})$ in order to obtain the normal and depth of $\mathcal{M}$.

Isometric mappings. Equation (19) gives three constraints:

$$\frac{E}{k^2} = \frac{\bar{E}}{\bar{k}^2} \quad \frac{F}{k^2} = \frac{\bar{F}}{\bar{k}^2} \quad \frac{G}{k^2} = \frac{\bar{G}}{\bar{k}^2}. \tag{29}$$

We differentiate these constraints under IP, using the expressions in equations (25) and (27), and obtain $(\bar{k}_1, \bar{k}_2)$ by solving the following equations:

$$\begin{aligned}
\bar{k}_1 &= \frac{\partial x^1}{\partial \bar{x}^1}k_1 + \frac{\partial x^2}{\partial \bar{x}^1}k_2 \\
&\quad - \frac{1}{2(E-F)}\left(\frac{\partial^2 x^1}{\partial\left(\bar{x}^1\right)^2}(A - C) + \frac{\partial^2 x^2}{\partial\left(\bar{x}^1\right)^2}(B - D)\right) \\
\bar{k}_2 &= \frac{\partial x^2}{\partial \bar{x}^1}k_1 + \frac{\partial x^2}{\partial \bar{x}^2}k_2 \\
&\quad - \frac{1}{2(F-G)}\left(\frac{\partial^2 x^1}{\partial\left(\bar{x}^2\right)^2}(A - C) + \frac{\partial^2 x^2}{\partial\left(\bar{x}^2\right)^2}(B - D)\right),
\end{aligned} \tag{30}$$

where A, B, C, D are given by equation (28).

Well-posedness: These expressions are linear and therefore $(\bar{k}_1, \bar{k}_2)$ can be uniquely determined, which leads to a unique solution of normals. $\bar{k}$ can also be uniquely determined by using the solution of $(\bar{k}_1, \bar{k}_2)$ in equation (29). Thus, isometric SfT possesses a unique solution under IP.

Stability of normals: In affine conditions, all second-order derivatives of the warp, $\dfrac{\partial x^1}{\partial \bar{x}^2}$, $\dfrac{\partial x^2}{\partial \bar{x}^1}$, F and $\bar{F}$ tend to vanish. In that case, the equations (30) are reduced to:

$$\bar{k}_1 = \frac{\partial x^1}{\partial \bar{x}^1}k_1 \qquad \bar{k}_2 = \frac{\partial x^2}{\partial \bar{x}^2}k_2. \tag{31}$$

This system is well-constrained and therefore, our solution to isometric SfT in equation (30) under IP is non-degenerate and stable in affine conditions.

Conformal mappings. Equation (20) gives three constraints:

$$\frac{1}{\bar{k}^2}\begin{pmatrix}\bar{E} & \bar{G} & \bar{F}\end{pmatrix} = \lambda^2 \frac{1}{k^2}\begin{pmatrix}E & G & F\end{pmatrix}, \tag{32}$$

where λ is the local scaling. On differentiating these expressions, we obtain $(\bar{k}_1, \bar{k}_2)$ as λ times the solution in equation (30). On canceling $(k, \bar{k})$ and λ in equation (32), we obtain:

$$E\bar{G} = \bar{E}G \quad F\bar{G} = \bar{F}G. \tag{33}$$

Using $(\bar{k}_1, \bar{k}_2)$ from the solution of equations (30) and the expressions of $(\bar{E}, \bar{F}, \bar{G})$ according to equation (24) in these equations, we obtain a unique solution for λ^2 given by:

$$\lambda^2 = \frac{FR - (G-E)S}{(2x^1k_1F - x^1k_2E - x^2k_1E)R - 2(x^1k_1G - x^2k_2E)S}, \tag{34}$$

where $R = (Gk_1^2 - Ek_2^2)$ and $S = k_1(Fk_1 - Ek_2)$.

Well-posedness: The solution to $(\bar{k}_1, \bar{k}_2)$ and λ obtained from equations (30) and (34) respectively is unique. Using $(\bar{k}_1, \bar{k}_2, \lambda)$ in equation (32), $\bar{k}$ can also be uniquely determined. In order to avoid sign flipping, we assume that $\lambda > 0$, and therefore it is uniquely determined.

Stability of normals: The solution to $(\bar{k}_1, \bar{k}_2)$ obtained from equations (30) does not suffer from degeneracies. However λ cannot be estimated in affine conditions. As can be seen from equation (34) with some minor algebraic manipulations, its value will tend to 0 in these conditions. Importantly, this is a generic degeneracy of the problem and not a specific degeneracy of our method. It can be understood intuitively from the fact that the conformal scale will be coupled with the affine scale and the two will become indistinguishable.

Equiareal mappings. Equation (21) is the constraint for an equiareal mapping. By differentiating it, we obtain two first-order constraints:

$$\begin{aligned}
&\frac{EG}{k^4} - \frac{F^2}{k^4} = \frac{\bar{E}\bar{G}}{\bar{k}^4} - \frac{\bar{F}^2}{\bar{k}^4} \\
&\frac{\partial}{\partial \bar{x}^i}\left(\frac{\bar{E}}{k^2}\right)\frac{\bar{G}}{\bar{k}^2} + \frac{\bar{E}}{\bar{k}^2}\frac{\partial}{\partial \bar{x}^i}\left(\frac{\bar{G}}{k^2}\right) - 2\frac{\bar{F}}{\bar{k}^2}\frac{\partial}{\partial \bar{x}^i}\left(\frac{\bar{F}}{k^2}\right) = \\
&\left(\frac{\partial}{\partial x^1}\left(\frac{E}{k^2}\right)\frac{\partial x^1}{\partial \bar{x}^i} + \frac{\partial}{\partial x^2}\left(\frac{E}{k^2}\right)\frac{\partial x^2}{\partial \bar{x}^i}\right)\frac{G}{k^2} \\
&+ \left(\frac{\partial}{\partial x^1}\left(\frac{G}{k^2}\right)\frac{\partial x^1}{\partial \bar{x}^i} + \frac{\partial}{\partial x^2}\left(\frac{G}{k^2}\right)\frac{\partial x^2}{\partial \bar{x}^i}\right)\frac{E}{k^2} \\
&- 2\frac{F}{k^2}\left(\frac{\partial}{\partial x^1}\left(\frac{F}{k^2}\right)\frac{\partial x^1}{\partial \bar{x}^i} + \frac{\partial}{\partial x^2}\left(\frac{F}{k^2}\right)\frac{\partial x^2}{\partial \bar{x}^i}\right), \quad i \in \{1,2\}
\end{aligned} \tag{35}$$

Using the expressions of differentials from equations (25) and (27), the above-mentioned constraints are written as:

$$\begin{aligned}
&|\mathbf{J}_\eta|\left(\bar{k}_1 - \left(k_1\frac{\partial x^1}{\partial \bar{x}^1} + k_2\frac{\partial x^2}{\partial \bar{x}^1}\right)\right) = \\
&-\frac{\partial x^2}{\partial \bar{x}^2}\frac{\partial^2 x^1}{\partial\left(\bar{x}^1\right)^2} + \frac{\partial x^2}{\partial \bar{x}^1}\frac{\partial^2 x^2}{\partial\left(\bar{x}^1\right)^2} + \frac{\partial x^2}{\partial \bar{x}^1}\frac{\partial^2 x^1}{\partial \bar{x}^1\partial \bar{x}^2} - \frac{\partial x^1}{\partial \bar{x}^1}\frac{\partial^2 x^2}{\partial \bar{x}^1\partial \bar{x}^2} \\
&|\mathbf{J}_\eta|\left(\bar{k}_2 - \left(k_1\frac{\partial x^1}{\partial \bar{x}^2} + k_2\frac{\partial x^2}{\partial \bar{x}^2}\right)\right) = \\
&-\frac{\partial x^2}{\partial \bar{x}^2}\frac{\partial^2 x^1}{\partial \bar{x}^1\partial \bar{x}^2} + \frac{\partial x^2}{\partial \bar{x}^1}\frac{\partial^2 x^2}{\partial \bar{x}^1\partial \bar{x}^2} + \frac{\partial x^2}{\partial \bar{x}^1}\frac{\partial^2 x^1}{(\partial \bar{x}^2)} - \frac{\partial x^1}{\partial \bar{x}^1}\frac{\partial^2 x^2}{(\partial \bar{x}^2)}.
\end{aligned} \tag{36}$$

Well-posedness: The above expressions are linear in $(\bar{k}_1, \bar{k}_2)$ and thus normals can be uniquely determined. $\bar{k}$ can also be uniquely obtained by using this solution in equation (35).

Stability of normals: In affine conditions, equations (36) reduce to equations (31) which are well-constrained and therefore, the solution to equiareal SfT under IP is non-degenerate and stable in affine conditions.

Skewless mappings. Equation (22) gives the constraint as:

$$F^2\bar{E}\bar{G} = \bar{F}^2EG. \tag{37}$$

This expression is independent of $(k, \bar{k})$. By differentiating it, we obtain:

$$\begin{aligned}
&2F\left(\frac{\partial F}{\partial x^1}\frac{\partial x^1}{\partial \bar{x}^i} + \frac{\partial F}{\partial x^2}\frac{\partial x^2}{\partial \bar{x}^i}\right)\bar{E}\bar{G} + F^2\left(\frac{\partial \bar{E}}{\partial \bar{x}^i}\bar{G} + \bar{E}\frac{\partial \bar{G}}{\partial \bar{x}^i}\right) = \\
&2\bar{F}\frac{\partial \bar{F}}{\partial \bar{x}^i}EG + \bar{F}^2\left(\frac{\partial E}{\partial x^1}\frac{\partial x^1}{\partial \bar{x}^i} + \frac{\partial E}{\partial x^2}\frac{\partial x^2}{\partial \bar{x}^i}\right)G \\
&+ \bar{F}^2E\left(\frac{\partial G}{\partial x^1}\frac{\partial x^1}{\partial \bar{x}^i} + \frac{\partial G}{\partial x^2}\frac{\partial x^2}{\partial \bar{x}^i}\right), \qquad i \in \{1,2\}
\end{aligned} \tag{38}$$

We expand these expressions using equations (25) and (27) and obtain:

$$\begin{aligned}
&EF\left(\bar{E}\bar{G} - \bar{F}^2\right)\left(\frac{\partial x^1}{\partial \bar{x}^2}k_1 + \frac{\partial x^2}{\partial \bar{x}^2}\right) - \bar{F}\bar{E}(EG - F^2)\bar{k}_2 = \\
&F\bar{E}\bar{G}\left(\frac{\partial^2 x^1}{\partial \bar{x}^1\partial \bar{x}^2}A + \frac{\partial x^2}{\partial \bar{x}^1\partial \bar{x}^2}B + \frac{\partial^2 x^1}{\partial\left(\bar{x}^1\right)^2}C + \frac{\partial x^2}{\partial\left(\bar{x}^1\right)^2}D\right) \\
&\bar{F}^2\left(E\left(\frac{\partial^2 x^1}{\partial \bar{x}^1\partial \bar{x}^2}C + \frac{\partial x^2}{\partial \bar{x}^1\partial \bar{x}^2}D\right) + G\left(\frac{\partial^2 x^1}{\partial\left(\bar{x}^1\right)^2}A + \frac{\partial x^2}{\partial\left(\bar{x}^1\right)^2}B\right)\right) \\
&GF\left(\bar{E}\bar{G} - \bar{F}^2\right)\left(\frac{\partial x^1}{\partial \bar{x}^1}k_1 + \frac{\partial x^2}{\partial \bar{x}^1}\right) - \bar{F}\bar{G}(EG - F^2)\bar{k}_1 = \\
&F\bar{E}\bar{G}\left(\frac{\partial^2 x^1}{\partial \bar{x}^1\partial \bar{x}^2}C + \frac{\partial x^2}{\partial \bar{x}^1\partial \bar{x}^2}D + \frac{\partial^2 x^1}{\partial\left(\bar{x}^2\right)^2}A + \frac{\partial x^2}{\partial\left(\bar{x}^2\right)^2}B\right) \\
&\bar{F}^2\left(G\left(\frac{\partial^2 x^1}{\partial \bar{x}^1\partial \bar{x}^2}A + \frac{\partial x^2}{\partial \bar{x}^1\partial \bar{x}^2}B\right) + E\left(\frac{\partial^2 x^1}{\partial\left(\bar{x}^2\right)^2}C + \frac{\partial x^2}{\partial\left(\bar{x}^2\right)^2}D\right)\right),
\end{aligned} \tag{39}$$

where A, B, C and D are given by equation (28). Using equation (37) in the above expressions, we obtain the following two constraints for skewless deformation:

$$\begin{aligned}
&F\bar{E}\bar{k}_2 - E\bar{F}\left(k_1\frac{\partial x^1}{\partial \bar{x}^2} + k_2\frac{\partial x^2}{\partial \bar{x}^2}\right) + \bar{F}(K + |\mathbf{J}_\eta|^{-1}MF) = 0 \\
&F\bar{G}\bar{k}_1 - G\bar{F}\left(k_1\frac{\partial x^1}{\partial \bar{x}^1} + k_2\frac{\partial x^2}{\partial \bar{x}^1}\right) + \bar{F}(L + |\mathbf{J}_\eta|^{-1}NF) = 0.
\end{aligned} \tag{40}$$

where:

$$\begin{aligned}
K &= C\frac{\partial^2 x^1}{(\partial x^1)^2} + D\frac{\partial^2 x^2}{(\partial x^1)^2} + A\frac{\partial^2 x^1}{\partial x^1\partial x^2} + B\frac{\partial^2 x^2}{\partial x^1\partial x^2}, \\
L &= C\frac{\partial^2 x^1}{\partial x^1\partial x^2} + D\frac{\partial^2 x^2}{\partial x^1\partial x^2} + A\frac{\partial^2 x^1}{(\partial x^2)^2} + B\frac{\partial^2 x^2}{(\partial x^2)^2}, \\
M &= -\frac{\partial x^2}{\partial \bar{x}^2}\frac{\partial^2 x^1}{(\partial x^1)^2} + \frac{\partial x^1}{\partial \bar{x}^2}\frac{\partial^2 x^2}{(\partial x^1)^2} + \frac{\partial x^2}{\partial \bar{x}^1}\frac{\partial^2 x^1}{\partial x^1\partial x^2} - \frac{\partial x^1}{\partial \bar{x}^1}\frac{\partial^2 x^2}{\partial x^1\partial x^2}, \\
N &= -\frac{\partial x^2}{\partial \bar{x}^2}\frac{\partial^2 x^1}{\partial x^1\partial x^2} + \frac{\partial x^1}{\partial \bar{x}^2}\frac{\partial^2 x^2}{\partial x^1\partial x^2} + \frac{\partial x^2}{\partial \bar{x}^1}\frac{\partial^2 x^1}{(\partial x^2)^2} - \frac{\partial x^1}{\partial \bar{x}^1}\frac{\partial^2 x^2}{(\partial x^2)^2},
\end{aligned} \tag{41}$$

and A, B, C and D are given by equation (28).

Well-posedness: The above expressions are cubic in $(\bar{k}_1, \bar{k}_2)$ and therefore normals cannot be uniquely determined. We pick the solution that minimizes the expression (37). $\bar{k}$ cannot be found in this case as the constraint (37) is independent of $(k, \bar{k})$.

Stability of normals: In affine conditions, the equations (40) vanish as both F and $\bar{F}$ tend to be zero. Thus skewless SfT under IP suffers from degeneracies and becomes non-stable.

4.3 Solutions using Connections

We use the geometric properties of connections to obtain a solution to SfT which does not use the MT-based formulation of deformation models. We use both IP and IL. For an IL mapping $\psi : \mathcal{T} \to \mathcal{M}$, according to corollary 2 the connection forms are preserved. Therefore, in figure 5 the connections at $\mathcal{T}$ (parametrized with x^1 and x^2) are related to the connections at $\mathcal{M}$ (parametrized with $\bar{x}^1$ and $\bar{x}^2$) by a change of variable given by equation (18) for any diffeomorphic IL mapping ψ between them. The components of these connection forms under a change of variable are:

$$\begin{aligned}\begin{pmatrix}\bar{\Gamma}^k_{11} & \bar{\Gamma}^k_{12}\\ \bar{\Gamma}^k_{21} & \bar{\Gamma}^k_{22}\end{pmatrix} &= \frac{\partial \bar{x}^k}{\partial x^1}\mathbf{J}_\eta^{-1}\begin{pmatrix}\Gamma^1_{11} & \Gamma^1_{12}\\ \Gamma^1_{21} & \Gamma^1_{22}\end{pmatrix}\mathbf{J}_\eta \\ &+ \frac{\partial \bar{x}^k}{\partial x^2}\mathbf{J}_\eta^{-1}\begin{pmatrix}\Gamma^2_{11} & \Gamma^2_{12}\\ \Gamma^2_{21} & \Gamma^2_{22}\end{pmatrix}\mathbf{J}_\eta + \mathbf{J}_\eta^{-1}\frac{\partial \mathbf{J}_\eta}{\partial x^k},\end{aligned} \tag{42}$$

where $k \in \{1, 2\}$. Under IP, the components of the connection forms are evaluated using equation (13). For $\mathcal{T}$ and $\mathcal{M}$, these expressions are written only in terms of (k_1, k_2) and $(\bar{k}_1, \bar{k}_2)$ respectively. This gives the following constraints:

$$\begin{aligned}\bar{k}_1 &= \frac{\partial x^1}{\partial \bar{x}^1}k_1 + \frac{\partial x^2}{\partial \bar{x}^1}k_2 - \frac{\partial \bar{x}^2}{\partial x^1}\frac{\partial^2 x^1}{\partial \bar{x}^1 \bar{x}^2} - \frac{\partial \bar{x}^2}{\partial x^2}\frac{\partial^2 x^2}{\partial \bar{x}^1 \bar{x}^2}\\ \bar{k}_2 &= \frac{\partial x^1}{\partial \bar{x}^2}k_1 + \frac{\partial x^2}{\partial \bar{x}^2}k_2 - \frac{\partial \bar{x}^1}{\partial x^1}\frac{\partial^2 x^1}{\partial \bar{x}^1 \bar{x}^2} - \frac{\partial \bar{x}^1}{\partial x^2}\frac{\partial^2 x^2}{\partial \bar{x}^1 \bar{x}^2}.\end{aligned} \tag{43}$$

Well-posedness: The above expressions are linear in $(\bar{k}_1, \bar{k}_2)$ and therefore normals can be uniquely determined. However, depth cannot be obtained as the above constraints are independent of $(k, \bar{k})$. Therefore, there exists a unique SfT solution for any deformation due to an IL mapping.

Stability of normals: In affine conditions, the equations (43) are reduced to (31) which is well-constrained and therefore, this solution is non-degenerate and stable.

Discussion: (Bartoli and Özgür, 2016) solves non-isometric SfT by minimizing the second-order derivatives of the surface. For a function $\mathbf{z}$ described in equation (1), it tries to minimize $\mathrm{d}^2\mathbf{z}$. Using equations (3), (4) and (5), we write:

$$\mathrm{d}^2\mathbf{z} = \mathrm{d}\left(\mathbf{e}_1\mathrm{d}x^1 + \mathbf{e}_2\mathrm{d}x^2\right) = \mathrm{d}\mathbf{e}_1\mathrm{d}x^1 + \mathrm{d}\mathbf{e}_2\mathrm{d}x^2. \tag{44}$$

Therefore, this solution tries to minimize $(\mathrm{d}\mathbf{e}_1, \mathrm{d}\mathbf{e}_2)$ whereas our solution in equation (43) is obtained by imposing a structure to $(\mathrm{d}\mathbf{e}_1, \mathrm{d}\mathbf{e}_2)$ using connection forms' components in equation (6). This is the underlying difference between the two methods. This structure of $(\mathrm{d}\mathbf{e}_1, \mathrm{d}\mathbf{e}_2)$ cannot be studied without the theory of connections which makes our framework complete.

Combining deformation modeling with connections. All SfT solutions that we proposed have a unique and a stable solution except for skewless SfT which is non-stable and non-unique. If we combine the SfT solution for IL mappings with the skewless SfT solution in equation (40), we obtain:

$$\begin{aligned}&(F\bar{E} - E\bar{F})\bar{k}_2\\ &+ \bar{F}\left(E\left(\frac{\partial \bar{x}^1}{\partial x^1}\frac{\partial^2 x^1}{\partial \bar{x}^1 \bar{x}^2} + \frac{\partial \bar{x}^1}{\partial x^2}\frac{\partial^2 x^2}{\partial \bar{x}^1 \bar{x}^2}\right) + K + |\mathbf{J}_\eta|^{-1}MF\right) = 0\\ &(F\bar{G} - G\bar{F})\bar{k}_1\\ &+ \bar{F}\left(G\left(\frac{\partial \bar{x}^2}{\partial x^1}\frac{\partial^2 x^1}{\partial \bar{x}^1 \bar{x}^2} + \frac{\partial \bar{x}^2}{\partial x^2}\frac{\partial^2 x^2}{\partial \bar{x}^1 \bar{x}^2}\right) + L + |\mathbf{J}_\eta|^{-1}NF\right) = 0.\end{aligned} \tag{45}$$

These equations are also cubic in $(\bar{k}_1, \bar{k}_2)$ and yield a non-unique and non-stable solution to normals. Skewless deformations are more inclusive than the rest of the deformations shown in figure 2 but they are loosely-constrained. Therefore, a connection-based SfT solution for IL mappings is interesting as it maintains the uniqueness and stability of the more constrained deformation modeling based SfT solutions: isometric, conformal, equiareal. It is also inclusive of all the mappings discussed in this paper and more.

Our findings on template-based 3D reconstruction of deformable objects are summarized in table 1.

4.4 Reconstruction Algorithm

We expressed the reconstruction equations for all deformation models in equations (30), (36), (40) and (43). All of these equations are expressed in terms of the unknowns $(\bar{k}_1, \bar{k}_2)$. We present the following algorithm to solve these equations.

Inputs: The warp η and (k, k_1, k_2) on the corresponding points of $\mathcal{T}$ and $\mathcal{M}$.

1) Densify corresponding points. Select a grid of points on the template and using the warps η, find the corresponding grid in the image. We used a 20×20 grid.

2) Find $(\bar{k}_1, \bar{k}_2)$. For isometric and conformal deformations, the solution to equation (30) gives $(\bar{k}_1, \bar{k}_2)$ linearly. For skewless deformations, equations (40) are cubic in $(\bar{k}_1, \bar{k}_2)$. We solve them by minimizing their sum-of-squares using (Henrion and Lasserre, 2003). For equiareal and IL deformations, equations (36) and (43) are also linear in $(\bar{k}_1, \bar{k}_2)$.

3) Find normals at $\mathcal{M}$. Compute the unit normal at each point on $\mathcal{M}$ according to equation (12) in terms of $(\bar{k}_1, \bar{k}_2)$.

4) Find depth at $\mathcal{M}$. Compute the up-to-scale depth by integrating the normals using the method proposed in (Chhatkuli et al., 2017b). For isometric, conformal and equiareal deformations, the scale can be evaluated by using $(\bar{k}_1, \bar{k}_2)$ in equations (29), (32) and (35) respectively.

Outputs: Reconstructed points and normals.

5 Template-Free Deformable 3D Reconstruction

We used our MT-CC framework to model and solve template-free deformable 3D reconstruction, commonly known as NRSfM. We present solutions for the deformation models discussed in section 3 under IP for isometric deformations. Other deformation models use both IL and IP to obtain a solution. While template-based reconstruction methods used either MT-based deformation modeling or connection-based modeling, template-free reconstruction is solved using both as there are more variables in this scenario than the former case.

5.1 General Model

Figure 6 shows the model. We have N input images $\mathcal{I}_1, \ldots, \mathcal{I}_N$ representing different deformations of the same object $\mathcal{M}_1, \ldots, \mathcal{M}_N$ viewed in a perspective camera. Our goal is to reconstruct the surfaces viewed in the N images.

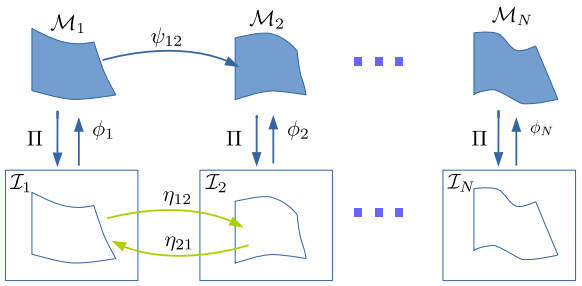

Fig. 6: Modeling N views of a deforming 3D surface.

	Deformation	Assumption	Degree	Depth	Normals	Solution	Stability
Template-based	Isometric	IP	1	Yes	Yes	Unique	Yes
	Conformal	IP	1	Yes	Yes	Unique	No
	Skewless	IP	3	No	Yes	Not unique	No
	Skewless	IP+IL	3	No	Yes	Not unique	No
	Equiareal	IP	1	Yes	Yes	Unique	Yes
	Generic	IP+IL	1	No	Yes	Unique	Yes
Template-free	Isometric	IP	3	No	Yes	Unique for >2 views	Yes
	Conformal	IP+IL	3	No	Yes	Unique for >2 views	Yes
	Skewless	IP+IL	5	No	Yes	Unique for >3 views	No
	Equiareal	IP+IL	3	No	No	--	--
	Generic	IP+IL	1	No	No	--	--

TABLE 1: Summary of template-based and template-free deformable 3D reconstruction for non-degenerate inputs. For each deformation model, we obtain constraints in two variables. The degree of these constraints, recoverability of depth and normals and the stability of normals is shown.

η_{ij} represents the image warp between the pair of images ($\mathcal{I}_i$, $\mathcal{I}_j$). ψ_{ij} is the deformation mapping between $\mathcal{M}_i$ and $\mathcal{M}_j$ modeled using the image embedding ϕ. We write the constraints for a pair of views i and j. This modeling can be extended to any number of image pairs. The moving frames (e_1^i, e_2^i, e_3^i) and $(\bar{e}_1, \bar{e}_2, \bar{e}_3)$ on $\mathcal{M}_i$ and $\mathcal{M}_j$ are written according to equation (12). The expressions (E_i, F_i, G_i), $(\bar{E}, \bar{F}, \bar{G})$ and their first-order derivatives are expressed according to equations (24) and (25). Using equation (26), we can write (e_1, e_2) at $\mathcal{M}_i$ which allows us to write (E, G, F) and its derivatives with respect to $(\bar{x}_1, \bar{x}_2)$. In this case, we can write the reconstruction equations in a similar fashion as the previous section but the unknowns are both (k_1, k_2, k) and $(\bar{k}_1, \bar{k}_2, \bar{k})$. The connections at $\mathcal{M}_i$ and $\mathcal{M}_j$ are preserved for isometric deformations using corollary 1 under IP. For the other deformations, they are preserved using corollary 2. Using the change of variable of equation (42), the connections at $\mathcal{M}_i$ and $\mathcal{M}_j$ can be defined in the same parametrization space. Therefore, we can express $(\bar{k}_1, \bar{k}_2, \bar{k})$ in terms of (k_1, k_2, k) using equation (43) which allows us to restrict the unknowns to (k_1, k_2, k) only.

5.2 Reconstruction Equations

Isometric/conformal mappings. Given that ψ is an isometric or a conformal mapping, from equations (29) and (32) the reconstruction equations for a pair of views $\mathcal{I}_i$ and $\mathcal{I}_j$ are given in equation (33) as a set of two cubic expressions in terms of (k_1, k_2) and $(\bar{k}_1, \bar{k}_2)$. Therefore isometry and conformity share the same constraints in the context of NRSfM. Substituting equation (43) in equation (33), we obtain two cubic equations in terms of (k_1, k_2) only. We proposed a solution to these equations for isometric deformations in (Parashar et al., 2017). It is important to note that this solution uses CS and therefore it could not be extended to conformal deformations.

Well-posedness: The above expressions are cubic in $(\bar{k}_1, \bar{k}_2)$, normals can be uniquely determined if more than 3 views are used. $\bar{k}$ cannot be found in this case as the constraint (33) is independent of $(k, \bar{k})$.

Stability of normals: Under affine conditions, the second constraint in (33) vanishes as both F and $\bar{F}$ tend to be zero which makes the system less-constrained. Therefore, it may need more than 3 views to recover a unique, stable solution.

Equiareal mappings. The reconstruction equations (36) are in terms of (k_1, k_2) and $(\bar{k}_1, \bar{k}_2)$. Using equation (43) in equation (36) leads to a system of equations independent of $(\bar{k}_1, \bar{k}_2)$ and (k_1, k_2). Therefore, these expressions cannot be used to solve for (k_1, k_2). We formalize this fact in the following theorem, proved in appendix E.

Theorem 4 (Non-solvability of Equiareal NRSfM)**.** *Equiareal NRSfM is not locally solvable.*

Skewless mappings. The reconstruction equations (40) are in terms of (k_1, k_2) and $(\bar{k}_1, \bar{k}_2)$. Using equation (43) in equation (40), we obtain two pentic equations in terms of (k_1, k_2) only. These equations can be solved by minimizing their sum-of-squares.

Well-posedness: The above expressions are pentic in $(\bar{k}_1, \bar{k}_2)$ and therefore normals can be uniquely determined if more than 4 views are used. $\bar{k}$ cannot be found in this case as the constraint (37) is independent of $(k, \bar{k})$.

Stability of normals: Under affine conditions both F and $\bar{F}$ tend to be zero and therefore constraints (40) tend to vanish. Therefore this solution suffers from degeneracies which makes it non-stable in affine conditions.

Infinitesimally linear mappings. If ψ is an IL mapping, there can only be two constraints obtained from equation (43) in terms of (k_1, k_2) and $(\bar{k}_1, \bar{k}_2)$ respectively. Thus, a solution for (k_1, k_2) cannot be obtained even under IL.

Our findings in template-free 3D reconstruction of deformable objects are summarized in table 1.

5.3 Reconstruction Algorithm

We expressed the reconstruction equations for all deformation models in equations (33), (36), (40) and (43). All of these equations are expressed in terms of the unknowns (k_1, k_2). We present the following algorithm to solve these equations:

Inputs: Warps η_{j1}, $j \in [2, N]$. The index 1 corresponds to the first image in the sequence. It can be chosen arbitrarily.

1) Densify corresponding points. Select a grid of points on the template and using the warps η_{1j}, find the corresponding grid in the image. We used a 20×20 grid.

2) Find (k_1, k_2). For isometric, conformal and skewless deformations, the solution to equations (33) and (40) gives (k_1, k_2). We solve these equations by minimizing their sum-of-squares using (Henrion and Lasserre, 2003).

3) Find $(\bar{k}_1, \bar{k}_2)$. $(\bar{k}_1, \bar{k}_2)$ can be expressed in terms of (k_1, k_2) and the first and second-order derivatives of η_{ji} using equation (43).

4) Find normals at $\mathcal{M}$. Compute the unit normal at each point on $\mathcal{M}$ using equation (12) in terms of $(\bar{k}_1, \bar{k}_2)$ and (k_1, k_2).

5) Find depth at $\mathcal{M}$. Use (Chhatkuli et al., 2017b).
Outputs: Reconstructed points and normals.

6 Experiments and Discussion

We tested our proposed SfT and NRSfM methods on two synthetic datasets, *Cylinder* and *Rubber* (Özgür and Bartoli, 2016); and four real datasets, *Paper* (Varol et al., 2012), *Balloon*, *Sock* and *Tissue* (Bartoli and Özgür, 2016). These datasets show objects undergoing different types of deformation. The *Balloon* and *Sock* datasets were recorded using Kinect2.0 and the point tracks were obtained using (Sundaram et al., 2010). A few images are shown in figure 7. We assume that the images are well-textured and register them using warps (Pizarro et al., 2016). However, any other technique, such as optical flow, that provides the first and second order derivatives of the image registration can be used instead. We also assume that the surfaces which are to be reconstructed are smooth.

For quantitative comparison, we measure the normal error (mean difference between computed and ground-truth normals in degrees) and the depth error (mean difference between computed and ground-truth 3D points in mm).

The proposed SfT solutions for isometric, conformal, equiareal and skewless deformation models are denoted by **IsoS**, **ConS**, **EqArS** and **SkewS** respectively. The proposed connection-based generic SfT solution is denoted by **GenS**. We compare our results with **IsoFS** (Bartoli et al., 2015), **ConFS** (Bartoli et al., 2015), **LinModS** (Salzmann and Fua, 2011) and **NoIsoS** (Bartoli and Özgür, 2016). (Bartoli and Özgür, 2016) proposed five solutions, we use the best one.

The proposed NRSfM solutions for isometric/conformal and skewless deformation models are denoted by **IsoConN** and **SkewN**. We compare our results with **MDHN** (Chhatkuli et al., 2017a) and **KerN** (Gotardo and Martinez, 2011).

Synthetic Datasets

Cylinder dataset. The cylinder dataset consists of images of a cylindrical surface deforming isometrically. These images are of size $640p \times 480p$ with a focal length of $400p$ with 400 point tracks. We added a random noise with a Gaussian distribution of 1 pixel standard deviation to the images. The mean normal and depth errors were evaluated from 20 trials. The results are shown in figure 7. The first four methods (**IsoConN**, **SkewN**, **MDHN** and **KerN**) are NRSfM methods. **IsoConN** shows the best performance amongst the NRSfM methods in this dataset. The images of this dataset do not come from a video sequence, therefore **KerN** did not do well for this dataset. In this dataset, the object and the camera do not move while deforming. (Chhatkuli et al., 2017a) reported this as a failure scenario for **MDHN** and therefore, it did not perform well for this dataset.

The SfT methods **IsoS**, **ConS**, **EqArS**, **GenS**, **IsoFS** and **ConFS** are all analytical solutions. Our SfT methods, **IsoS**, **ConS**, **EqArS** and **GenS** are all linear solutions that incorporate local smoothness. Therefore, they show better performance than **IsoFS** and **ConFS**. **SkewS** does not show good results on this dataset. This is because it is non-stable and not well-constrained. **IsoFS**, **ConFS** and **LinModS** show a similar good performance on this dataset. **NoIsoS** needs high perspective in images and therefore it performed very well in this dataset. The performance of this method is quite close to best performing SfT methods.

Performance of methods in noisy conditions. We evaluated the performance of the methods in noisy conditions. We added 1-5 pixels noise to the images of the dataset and obtain the results for each method. We report the normal and depth errors for each experiment averaged over 20 trials. Figure 8 shows our results. Our SfT (**IsoS**, **ConS**, **SkewS**, **EqArS**, **GenS**) and NRSfM (**IsoConN**, **SkewN**) methods show a very stable performance in noisy conditions. The performance of other methods is quite stable as well. Our methods exploit the first and second-order derivatives of the warps. These derivatives, especially the second-order ones, may be largely affected by the noise. Therefore, the methods **EqArS**, **GenS**, **IsoConN** which solve SfT/NRSfM in terms of the first and second-order derivatives of the warp show a larger increase in the errors compared to other methods such as **IsoFS** and **ConFS** that use the first-order derivatives of the warps only. **LinModS**, **NoIsoS**, **ConS** and **IsoS** are also quite stable in the presence of noise. The skewless methods **SkewN** and **SkewS** also show a good tolerance to noise even though their performance on this dataset is not so good. **MDHN** and **KerN** do not perform well and they are largely affected by noise as well.

Curvature test of our methods. The best performing methods on this dataset are **EqArS** and **GenS**, **GenS** being slightly better. These solutions are dependent on the first and second-order derivatives of the warps. The second-order derivatives may be non-stable. We corrected them by using the refinement method (Pizarro et al., 2016). However it may be difficult to find them in some cases, therefore it is interesting to see the performance of these methods without second-order derivatives. We make an approximation to the solution of **GenS** by disregarding the second-order derivatives. The new solution is called **GenS0**. Figure 9 shows the results of all methods with respect to the varying curvature of the surface. The curvature is the inverse of the radius. In this experiment we show reconstruction for 10 surfaces of the cylinder with the radius varying from 2 to 10. In general the reconstruction errors increase with bending. However, **IsoConN**, **SkewN** and **GenS** do not show a sharp increase in errors due to bending. **GenS0** is affected by bending, especially when it is strong, but it still shows decent results for highly bent surfaces.

The interesting thing about **GenS** is the simplicity of the solution. The reconstruction algorithm is only two lines of code given that (k_1, k_2) in equation (43) are obtained from the template. This means that the computational cost of this method is very low as it involves simple additions and multiplications only. Even by ignoring second-order derivatives, **GenS0** gives decent results.

Computation time comparison. Our SfT methods, except **SkewS**, are linear and therefore they are computationally very cheap. In general, for 20 images and 400 points on the cylinder dataset, it takes ≈ 5 seconds for these methods to evaluate the results. The computation time of other SfT methods is much higher: 20-50 seconds for **ConFS** and **IsoFS** and 150-190 seconds for **LinModS** and **NoIsoS**. The computation time for our NRSfM methods is about 20 seconds on

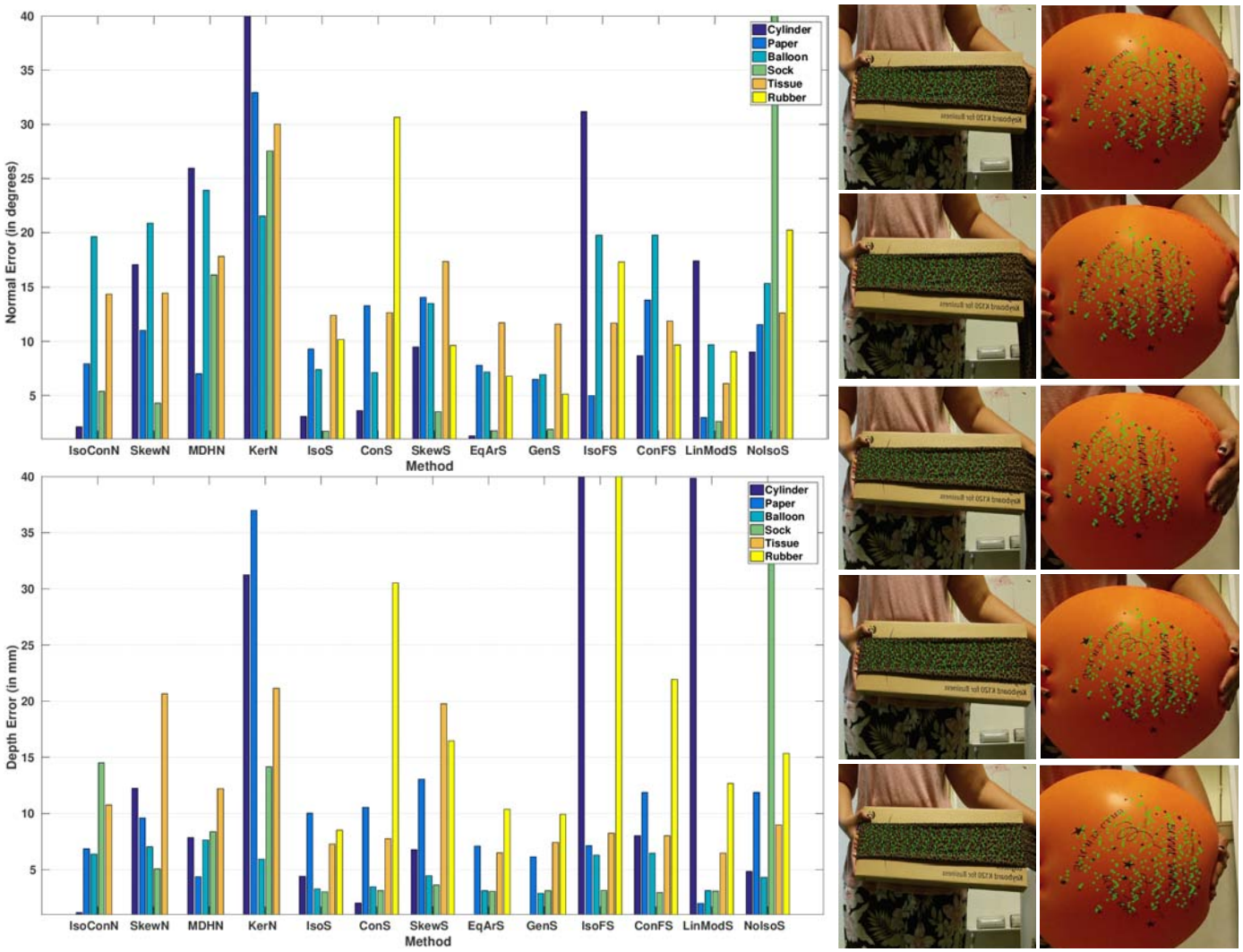

Fig. 7: (left) Normal and depth errors on all datasets. The errors shown are evaluated by averaging the errors on the entire image-set. The first four methods shown are NRSfM methods and the rest are SfT methods. In general, the performance of SfT methods is better than NRSfM methods on these datasets. The methods ending with N and S are NRSfM and SfT methods respectively. (right) Images from the sock and balloon datasets. Some of the tracked points are shown. Best viewed in colour.

this dataset which is quite faster than **MDHN** and **KerN**. Futhermore our NRSfM methods have a linear complexity and therefore, they are capable of handling a large number of images. **MDHN** and **KerN** have a non-linear complexity, therefore, reconstructing a large number of images can be very slow. Especially **MDHN**, which cannot reconstruct more than 50-60 images. Table 2 shows the computation time for all the compared methods on the cylinder dataset reported on a PC with an i5 CPU and 8 GB RAM.

Rubber dataset. It consists of 50 partially-stretched surfaces of a rubber with 400 point tracks. We evaluated all compared SfT and NRSfM methods on the first 20 images of this dataset. The rubber is partially stretched from its longest side in a sequential order. Figure 7 summarizes the performance of different methods on this dataset. The reconstruction of surfaces 10 and 20 by the compared methods are shown in figure 15 of appendix F. Amongst NRSfM methods, **IsoConN** shows the best performance. The rest of the NRSfM methods do not perform well. Amongst SfT methods, **LinModS** shows the best performance with **EqArS** and **GenS** being close in terms of depth. Figure 15 shows that the curvature of the surface 10 is best captured by **EqArS** with **GenS** whereas surface 20 is decently reconstructed by **LinModS** only. For low deformations of this dataset, **EqArS** with **GenS** show better results than **LinModS** but they cannot cope up with the higher deformations.

Real Datasets

Paper dataset. It consists of 190 images with 1500 point tracks of a paper deforming isometrically. We picked 20 images by uniformly sampling the dataset. Figure 7 summarizes the performance of the compared methods on this dataset. Amongst NRSfM methods, **MDHN** shows the best performance, with **IsoConN** being very close to it. **SkewN** also shows good results on this dataset. **KerN** does not have good results. Our SfT methods show a very good performance on this dataset. **NoIsoS** also leads to decent reconstruction in this dataset. However, **LinModS** shows the best performance. The reconstructions of two surfaces of this dataset are shown in figure 16 of appendix F. **IsoFS** and **ConFS** do not show a good performance on the selected

Method	IsoConN	SkewN	MDHN	KerN	IsoS	ConS	SkewS	EqArS	GenS	IsoFS	ConFS	LinModS	NoIsoS
Time (in sec)	20.0	42.3	52.7	56.4	4.3	5.4	201.5	4.5	3.3	55.6	23.5	148.7	190.9

TABLE 2: Computation time comparison of all the methods on 20 images of the cylinder dataset with 400 tracked points.

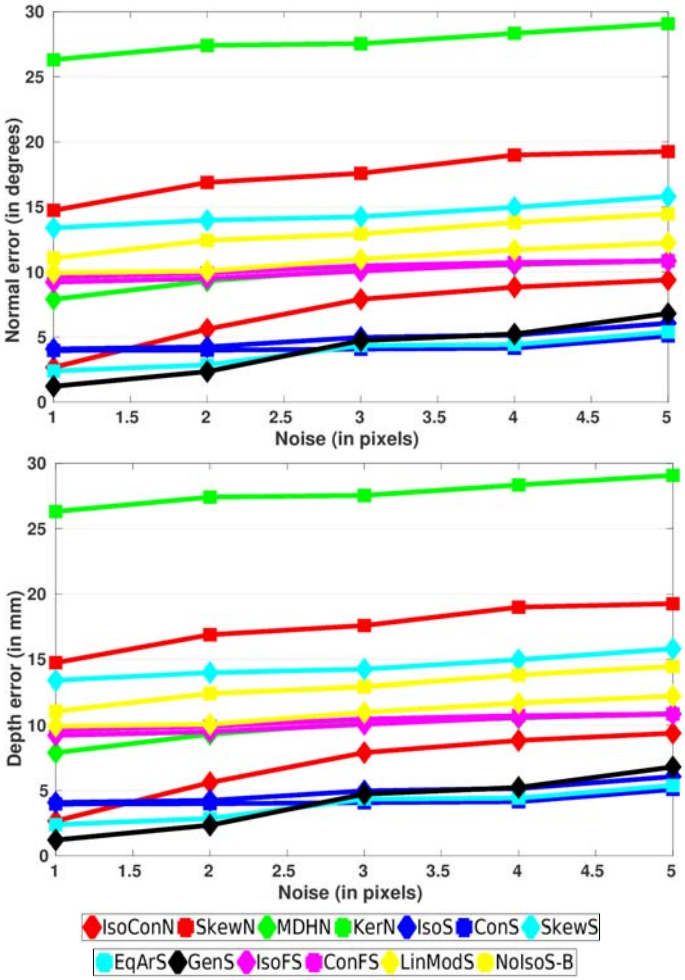

Fig. 8: Normal and depth errors on the cylinder dataset by varying the noise from 1 to 5 pixels. Best viewed in colour.

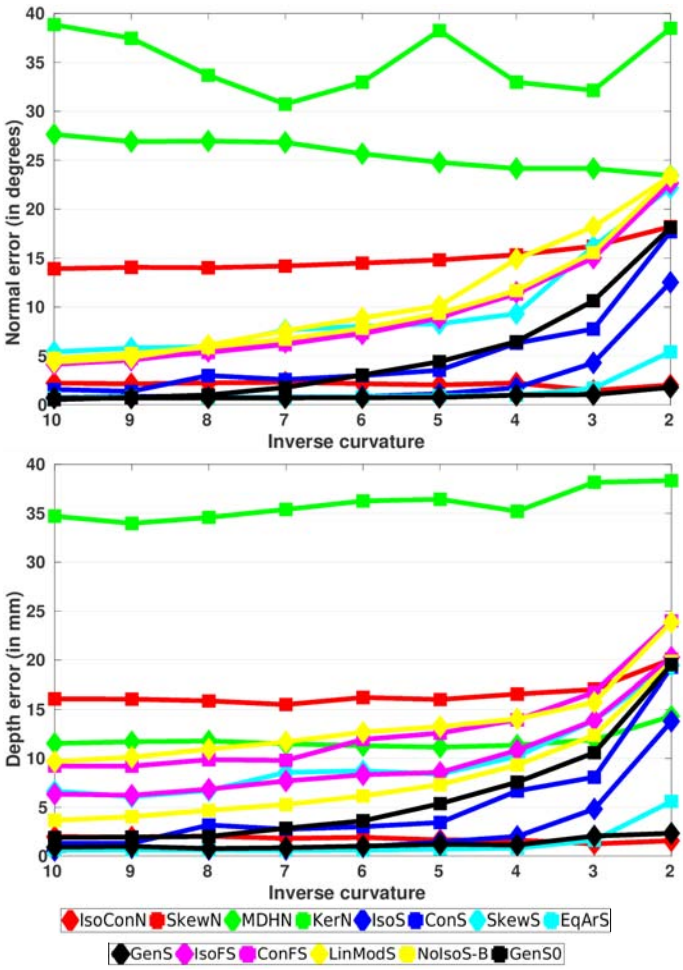

Fig. 9: Normal and depth errors on the cylinder dataset by varying the radius from 2 to 10. The surface with radius 2 is the most curved. Best viewed in colour.

images of this dataset. We recall that in order to compare them with our methods, we do not perform the refinement step proposed for these methods. This is because our goal is to compare the analytical solutions of these methods to ours. **MDHN** and **LinModS** both perform a global convex optimization whereas our methods **IsoConN** and **IsoS** yield a local and analytical solution. Global coherence is thus not guaranteed but could be added by coupling our methods with the non-convex optimization proposed in (Chhatkuli et al., 2017b), which showed a significant performance boost and achieved better results than **LinModS** when combined with **IsoFS**.

Balloon dataset. It consists of 20 images uniformly sampled from a video sequence of 80 images with 3000 point tracks. We find that the mean normal error for all NRSfM methods on this dataset is around 20 degrees which is very high as compared to the performance of these methods on other datasets. However, the mean depth error for these methods is quite comparable to the rest of the datasets. This indicates the flattening of the reconstructed surface. However, **IsoConN** shows the best performance amongst compared NRSfM methods. Our SfT methods except **SkewS** show a very good performance on this dataset and their results are very similar. The reconstruction from **SkewS** is quite flat. **IsoFS**, **ConFS** and **NoIsoS**, all of these methods also lead to flat reconstructions. **LinModS** performed quite well on this dataset. Its performance is close to **EqArS** and **GenS** which are the best performing methods on this dataset. This dataset is near-affine. Thus, most of the methods did not do well. The reconstruction of two surfaces using the compared methods is shown in figure 17 of appendix F.

Sock dataset. It consists of 20 images with 3500 point tracks. The sock undergoes elastic deformations in one direction only. Analytical methods show a very good performance on this dataset. Amongst NRSfM methods, **SkewN** showed the best performance as the sock is undergoing almost skewless

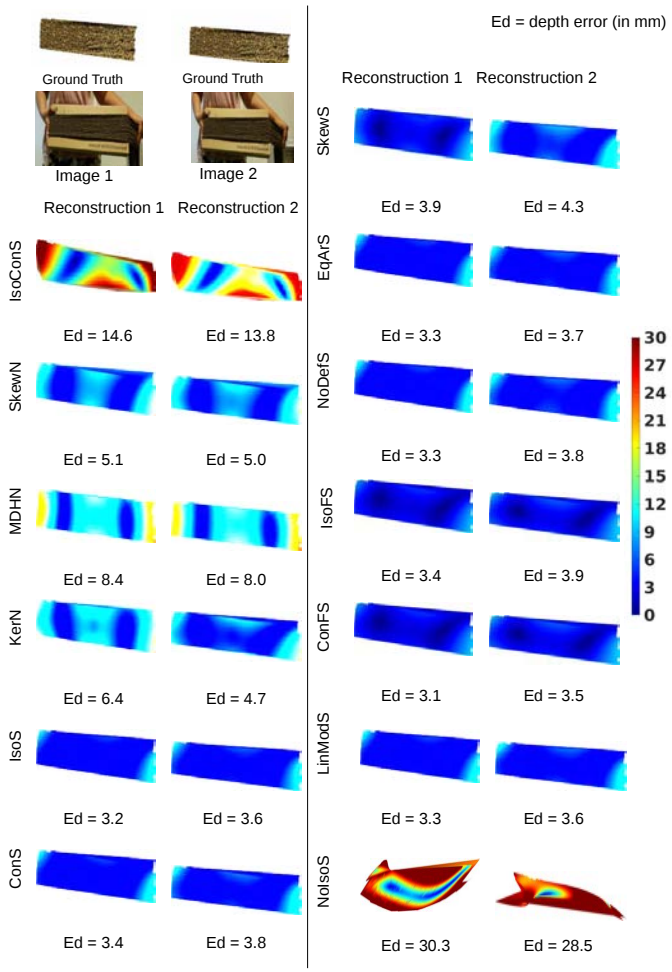

Fig. 10: Error maps for two surfaces of the sock dataset. The depth error maps show the difference in the reconstruction and ground truth. Best viewed in colour.

deformation. The reconstruction of normals by **IsoConN** is quite good but it cannot cope with the stretching of the surface and therefore, it leads to a higher depth error. **MDHN** and **KerN** did not do well on this dataset. SfT methods except **NoIsoS**, which completely broke on this dataset, showed a very good reconstruction even though the object was stretched. **GenS** shows the best performance. However, the rest of the methods are quite competitive. An important thing to note is that even though **IsoFS** and **ConFS** show the best performance in computing normals, their computation of depth is not as good as **IsoS** and **ConS**. This is because **IsoS** and **ConS** use the constraints of **IsoFS** and **ConFS**, given in equation (29), along with additional constraints obtained in equation (30) which gives **IsoS** and **ConS** the liberty to reconstruct stretched surfaces better. The reconstruction of two surfaces of this dataset using the compared methods is shown in figure 10.

Tissue dataset. It is a piece of elastic tissue with 100 points matched to an undeformed template of the tissue. It has only one image. Therefore only SfT methods could be compared for this dataset. **GenS** shows the best performance on this dataset with the rest of the methods, except **SkewS**, **ConS** and **NoIsoS**, being close enough to the best solution. The reconstruction of the tissue using the compared methods is shown in figure 18 of appendix F.

Discussion on generic solutions. An important point to note here is that **NoIsoS** and **GenS** both reconstruct the surface without modeling deformation explicitly. However, we found **NoIsoS**, which uses a differential framework, to be non-stable. (Bartoli and Özgür, 2016) proposed five solutions to cope with the stability issue. The main idea of this method is to use smoothness (expressed in terms of the second-order differentials of the surface) in order to reconstruct surfaces. Also, it needs the input image to have a high amount of perspective in order to give decent results. Our solution to **GenS** (along with other solutions) also relies on the second-order derivatives of the surfaces under the assumption of IL. Our experiments show that however our solution to **GenS** is stable.

Discussion on missing data, occlusions and self-occlusions. Since our proposed framework is local, it naturally handles missing data and occlusions. We used CVLAB's occluded paper dataset, which adds an occlusion mask to the paper dataset as shown in figure 11, and evaluated all methods. All SfT methods could handle the occlusion and their performance was similar to the paper dataset without occlusions which is reported in figure 7. Our proposed NRSfM methods, **IsoConN** and **SkewN**, are also almost unaffected by the occlusion and they reconstruct the entire paper despite the occlusion. Figure 11 shows the result. **KerN** fails to reconstruct the surfaces with missing data due to occlusion. Figure 11 also shows that **MDHN** could not reconstruct the occluded portion on the paper but it managed to reconstruct the rest of the paper with almost the same accuracy as the reported one in figure 7. Strictly speaking, it cannot handle occlusions but unlike **KerN**, it manages to reconstruct the portion of the surfaces unaffected by the occlusion.

Dealing with self-occluded surfaces is rather a practical problem than a theoretical one. The challenging task is their registration which is a difficult problem. However, there exists previous work which propose solutions to register such surfaces.

Discussion on learning-based reconstruction methods. Recently, (Pumarola et al., 2018) proposed **DeformNet**, a learning-based solution to SfT and evaluated its performance on the Paper dataset. It reported a reconstruction error of $2.7mm$, whereas our method **IsoS** yields an error $6.5mm$. A performance similar to **DeformNet** can be obtained by coupling **IsoS** with a refinement method such as (Chhatkuli et al., 2017b). Unlike **IsoS** or (Chhatkuli et al., 2017b), (Pumarola et al., 2018) requires the network to be trained using the 3D surface ground truth of the dataset to be tested on. The Paper dataset is recorded using the RGBD Kinect sensor and therefore, the ground truth is available for it. This is a strong practical limitation as the ground truth is non-feasibly computable in most real scenarios like medical endoscopies where the data is recorded using regular RGB cameras only.

Summary of experiments. The results of all the compared methods on each dataset are summarized in figure 7. On these datasets, the best performing NRSfM methods are **IsoConN** and **MDHN**. While our methods have a linear computational complexity, **MDHN** performs a convex optimization with cubic computational complexity which takes it almost an hour to reconstruct 50-60 images. Therefore,

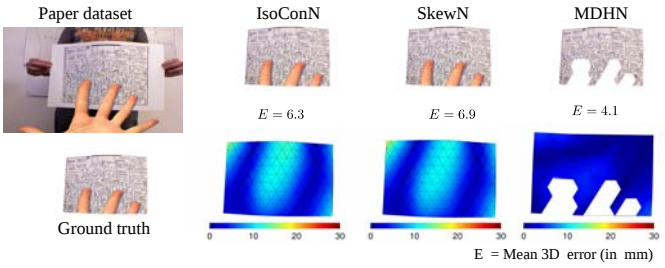

Fig. 11: Image renderings and error maps of the reconstruction of paper dataset under occlusion. Our NRSfM methods manage to reconstruct complete surfaces despite occlusions which **MDHN** cannot. Best viewed in colour.

it is highly unscalable. For SfT methods, our methods (except **SkewS**) showed a very good performance on all the datasets. **GenS** showed the best performance on most of the datasets. **LinModS** showed a very good performance on these datasets, it showed the best performance in the rubber and paper datasets. However, **GenS** and **EqArS** have been very competitive with **LinModS**. **SkewN** gives very good results on the sock dataset. **LinModS** performs a convex optimization while our methods are purely analytical.

7 Conclusions

We presented the MT-CC differential framework for deformable 3D reconstruction. We used this framework to find solutions to isometric, conformal, skewless and equiareal SfT under IP. Using this framework, we also proposed a generic solution to SfT under IL. We obtained solutions to isometric, conformal and skewless NRSfM under the assumption of IP using this framework. Our solution to conformal NRSfM is the same as isometric NRSfM. We showed that equiareal NRSfM cannot be solved locally. Our NRSfM methods solve the minimum data case, have linear complexity in the number of points, handle missing data as they reconstruct locally, work for both short and wide-baseline datasets, work with both large and small number of images. Our experiments showed that the proposed SfT and NRSfM methods outperform most of the compared methods in terms of accuracy and computation time. In future work, our goal is to study the deformable 3D reconstruction for all algebraic deformation models without using IP. So far we have only explored the affine CC. We now aim to study the nature of projective CC and how can they be used in deformable 3D reconstruction. Also, we would like to extend these methods to reconstruct non-smooth objects. The surface patches that are consistently smooth need to be identified and reconstructed independently. The complete reconstruction can then be obtained by sewing the independent reconstructions together.

Acknowledgements. This research has received funding from the EU's FP7 through the ERC grant 307483 FLEXABLE, the Spanish Ministry of Economy, Industry and Competitiveness under project ARTEMISA (TIN2016-80939-R).

References

A. Agudo and F. Moreno-Noguer. Simultaneous pose and non-rigid shape with particle dynamics. In *CVPR*, 2015.

A. Agudo, F. Moreno-Noguer, B. Calvo, and J. M. M. Montiel. Sequential non-rigid structure from motion using physical priors. *IEEE Transactions on Pattern Analysis and Machine Intelligence (TPAMI)*, 38(5):979–994, 2016.

I. Akhter, Y. Sheikh, S. Khan, and T. Kanade. Nonrigid structure from motion in trajectory space. In *NIPS*, 2009.

A. Bartoli and E. Özgür. A perspective on non-isometric shape-from-template. In *ISMAR*, 2016.

A. Bartoli, Y. Gérard, F. Chadebecq, T. Collins, and D. Pizarro. Shape-from-template. *IEEE Transactions on Pattern Analysis and Machine Intelligence*, 37(10):2099–2118, 2015.

V. Blanz and T. Vetter. Face recognition based on fitting a 3D morphable model. *IEEE Transactions on Pattern Analysis and Machine Intelligence*, 25(9):1063–1074, 2003.

C. Bregler, A. Hertzmann, and H. Biermann. Recovering non-rigid 3D shape from image streams. In *CVPR*, 2000.

F. Brunet, A. Bartoli, and R. Hartley. Monocular template-based 3D surface reconstruction: Convex inextensible and nonconvex isometric methods. *Computer Vision and Image Understanding*, 125:138–154, 2014.

C. Cagniart, E. Boyer, and S. Ilic. Free-form mesh tracking: a patch-based approach. In *CVPR*, 2010.

É. Cartan. Sur les variétés à connexion affine, et la théorie de la relativité généralisée (premier partie). *Annales Scientifiques de l'École Normale Supérieure*, 40:325–412, 1923.

É. Cartan. Sur les variétés à connexion projective. *Bulletin de la Société Mathématique*, 52:205–241, 1924.

É. Cartan. Espaces à connexion affine, projective et conforme. *Acta Mathematica*, 48:1–42, 1926.

É. Cartan. *La théorie des groupes finis et continus et la géométrie différentielle traitées par la méthode du repère mobile*. Paris: Gauthier-Villars, 1937. ISBN 978-0-12-088735-4.

É. Cartan. *Differential Forms*. Hermann, 1970. ISBN 978-0-12-088735-4.

A. Chhatkuli, D. Pizarro, and A. Bartoli. Non-rigid shape-from-motion for isometric surfaces using infinitesimal planarity. In *BMVC*, 2014.

A. Chhatkuli, D. Pizarro, T. Collins, and A. Bartoli. Inextensible non-rigid structure-from-motion by second-order cone programming. *IEEE transactions on Pattern Analysis and Machine Intelligence*, pages 1–1, 2017a.

A. Chhatkuli, D. Pizarro, T. Collins, and A. Bartoli. A stable analytical framework for isometric shape-from-template by surface integration. *IEEE Transactions on Pattern Analysis and Machine Intelligence*, 39(5):833–850, 2017b.

Y. Dai, H. Li, and M. He. A simple prior-free method for non-rigid structure-from-motion factorization. *International Journal of Computer Vision*, 107(2):101–122, 2014.

E. De Aguiar, C. Stoll, C. Theobalt, N. Ahmed, H.-P. Seidel, and S. Thrun. Performance capture from sparse multi-view video. *ACM Transactions on Graphics*, 27(3):98, 2008.

A. Del Bue, F. Smeraldi, and L. Agapito. Non-rigid structure from motion using non-parametric tracking and non-linear optimization. In *CVPRW*, 2004.

P. Gotardo and A. Martinez. Kernel non-rigid structure from motion. In *ICCV*, 2011.

N. Gumerov, A. Zandifar, R. Duraiswami, and L. S. Davis. Structure of applicable surfaces from single views. In *ECCV*, 2004.

N. Haouchine, J. Dequidt, M. Berger, and S. Cotin. Single

view augmentation of 3D elastic objects. In *ISMAR*, 2014.
R. I. Hartley and A. Zisserman. *Multiple View Geometry in Computer Vision*. Cambridge University Press, ISBN: 0521623049, 2000.
D. Henrion and J. B. Lasserre. Gloptipoly: Global optimization over polynomials with matlab and sedumi. *ACM Transactions on Mathematical Software*, 29(2):165–194, 2003.
M. Innmann, M. Zollhöfer, M. Nießner, C. Theobalt, and M. Stamminger. Volumedeform: Real-time volumetric non-rigid reconstruction. In *ECCV*, 2016.
A. Kock. *Synthetic Geometry of Manifolds.* Cambridge University Press, 2010. ISBN 978-0-521-11673-2.
A. Malti and C. Herzet. Elastic shape-from-template with spatially sparse deforming forces. In *CVPR*, 2017.
A. Malti, R. Hartley, A. Bartoli, and J.-H. Kim. Monocular template-based 3D reconstruction of extensible surfaces with local linear elasticity. In *CVPR*, 2013.
D. Mehta, O. Sotnychenko, F. Mueller, W. Xu, S. Sridhar, G. Pons-Moll, and C. Theobalt. Single-shot multi-person 3d pose estimation from monocular RGB. In *3DV*, 2018.
F. Moreno-Noguer, M. Salzmann, V. Lepetit, and P. Fua. Capturing 3D stretchable surfaces from single images in closed form. In *CVPR 2009*, 2009.
R. A. Newcombe, D. Fox, and S. M. Seitz. Dynamicfusion: Reconstruction and tracking of non-rigid scenes in real-time. In *CVPR*, 2015.
D. T. Ngo, S. Park, A. Jorstad, A. Crivellaro, C. D. Yoo, and P. Fua. Dense image registration and deformable surface reconstruction in presence of occlusions and minimal texture. In *ICCV*, 2015.
S. I. Olsen and A. Bartoli. Implicit non-rigid structure-from-motion with priors. *Journal of Mathematical Imaging and Vision*, 31(2-3):233–244, 2008.
B. O'Neill. *Elementary differential geometry.* Elsevier, 2006. ISBN 978-0-12-088735-4.
E. Özgür and A. Bartoli. Particle-SfT: a Provably-Convergent, Fast Shape-from-Template Algorithm. *International Journal of Computer Vision*, 123(2):184–205, 2016.
S. Parashar, D. Pizarro, and A. Bartoli. Isometric Non-Rigid Shape-from-Motion with Riemannian Geometry Solved in Linear Time. *IEEE Transactions on Pattern Analysis and Machine Intelligence*, 2017.
M. Perriollat, R. Hartley, and A. Bartoli. Monocular template-based reconstruction of inextensible surfaces. *International Journal of Computer Vision*, 95(2):124–137, 2011.
D. Pizarro, R. Khan, and A. Bartoli. Schwarps: Locally projective image warps based on 2D schwarzian derivatives. *International Journal of Computer Vision*, 119(2):93–109, 2016.
A. Pumarola, A. Agudo, L. Porzi, A. Sanfeliu, V. Lepetit, and F. Moreno-Noguer. Geometry-aware network for non-rigid shape prediction from a single view. In *CVPR*, 2018.
C. Russell, R. Yu, and L. Agapito. Video pop-up: Monocular 3d reconstruction of dynamic scenes. In *ECCV*, 2014.
M. Salzmann and P. Fua. Linear local models for monocular reconstruction of deformable surfaces. *IEEE Transactions on Pattern Analysis and Machine Intelligence*, 33(5):931–944, 2011.
J. Starck and A. Hilton. Model-based multiple view reconstruction of people. In *ICCV*, 2003.
N. Sundaram, T. Brox, and K. Keutzer. Dense point trajectories by gpu-accelerated large displacement optical flow. In *ECCV*, 2010.
J. Taylor, A. D. Jepson, and K. N. Kutulakos. Non-rigid structure from locally-rigid motion. In *CVPR*, 2010.
A. Tewari, M. Zollöfer, F. Bernard, P. Garrido, H. Kim, P. Perez, and C. Theobalt. High-fidelity monocular face reconstruction based on an unsupervised model-based face autoencoder. *IEEE Transactions on Pattern Analysis and Machine Intelligence*, PP:1–1, 2018.
L. Torresani, D. B. Yang, E. J. Alexander, and C. Bregler. Tracking and modeling non-rigid objects with rank constraints. In *CVPR*, 2001.
L. Torresani, A. Hertzmann, and C. Bregler. Nonrigid structure-from-motion: Estimating shape and motion with hierarchical priors. *IEEE Transactions on Pattern Analysis and Machine Intelligence*, 30(5):878–892, 2008.
A. Varol, M. Salzmann, E. Tola, and P. Fua. Template-free monocular reconstruction of deformable surfaces. In *ICCV*, 2009.
A. Varol, M. Salzmann, P. Fua, and R. Urtasun. A constrained latent variable model. In *CVPR*, 2012.
S. Vicente and L. Agapito. Soft inextensibility constraints for template-free non-rigid reconstruction. In *ECCV*, 2012.
X. Zhou, M. Zhu, G. Pavlakos, S. Leonardos, K. G. Derpanis, and K. Daniilidis. Monocap: Monocular human motion capture using a cnn coupled with a geometric prior. *IEEE Transactions on Pattern Analysis and Machine Intelligence*, 2018.
M. Zollhöfer, P. Stotko, A. Görlitz, C. Theobalt, M. Nießner, R. Klein, and A. Kolb. State of the art on 3D reconstruction with RGB-D cameras. In *Computer Graphics Forum*, 2018.

8 Biographies

Shaifali Parashar received her PhD degree in Computer Vision from Université Clermont Auvergne. She is currently a Post-doc researcher in CVLAB, EPFL. Her research interest are non-rigid 3D reconstruction.

Daniel Pizarro Pérez has been an Associate Professor at the Universidad de Alcalá (Spain) since 2012. He is a member of the GEINTRA group and an invited member of EnCoV group. His research interests include image registration, deformable reconstruction and their applications to minimally invasive surgeries.

Adrien Bartoli has been a Professor of Computer Science at Université d'Auvergne since fall 2009. He leads the EnCoV research group. He is a member of CNRS, Institut Pascal and CHU de Clermont-Ferrand. His research interests include image registration and Shape-from-X for rigid and non-rigid environments, with applications to computer-aided endoscopy.

APPENDIX A
CHRISTOFELL SYMBOLS PRESERVATION LAW

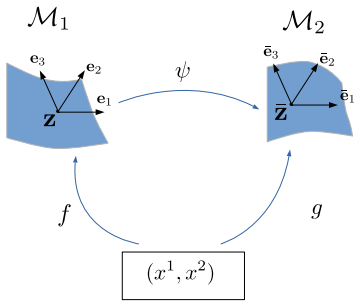

Fig. 12: Two surfaces $\mathcal{M}_1$ and $\mathcal{M}_2$ related by ψ are parametrized using (x^1, x^2).

We discuss how the CS transform across surfaces under any deformation model. Figure 12 shows two surfaces related by a mapping ψ. Given that $g = \psi \circ f$, the moving frames $(\mathbf{e}_1, \mathbf{e}_2, \mathbf{e}_3)$ and $(\bar{\mathbf{e}}_1, \bar{\mathbf{e}}_2, \bar{\mathbf{e}}_3)$ on the planes $\mathcal{M}_1$ and $\mathcal{M}_2$ are related by:

$$\begin{pmatrix}\bar{\mathbf{e}}_1 & \bar{\mathbf{e}}_2\end{pmatrix} = \mathbf{J}_{\psi\circ f}\begin{pmatrix}\mathbf{e}_1 & \mathbf{e}_2\end{pmatrix} = \begin{pmatrix}\mathbf{J}_{\psi\circ f}\mathbf{e}_1 & \mathbf{J}_{\psi\circ f}\mathbf{e}_2\end{pmatrix}. \tag{46}$$

The metric tensor $\bar{\mathbf{g}}$ at $\mathcal{M}_2$ is given by:

$$\bar{\mathbf{g}} = \begin{pmatrix}\bar{\mathbf{e}}_1^\top \\ \bar{\mathbf{e}}_2^\top\end{pmatrix}\begin{pmatrix}\bar{\mathbf{e}}_1 & \bar{\mathbf{e}}_2\end{pmatrix} = \begin{pmatrix}\mathbf{e}_1^\top \\ \mathbf{e}_2^\top\end{pmatrix}\mathbf{J}_{\psi\circ f}^\top\mathbf{J}_{\psi\circ f}\begin{pmatrix}\mathbf{e}_1 & \mathbf{e}_2\end{pmatrix}$$

where $\mathbf{J}_{\psi\circ f}^\top\mathbf{J}_{\psi\circ f}$

$$= \begin{cases}\mathbf{I} & \psi \text{ is isometric} \\ \begin{pmatrix}\lambda_1 & \lambda_4 & \lambda_5 \\ \lambda_4 & \lambda_2 & \lambda_6 \\ \lambda_5 & \lambda_6 & \lambda_3\end{pmatrix} & \text{otherwise}\end{cases} \tag{47}$$

Therefore, given the metric tensor $\mathbf{g} = \begin{pmatrix}\mathbf{e}_1 & \mathbf{e}_2\end{pmatrix}^\top\begin{pmatrix}\mathbf{e}_1 & \mathbf{e}_2\end{pmatrix}$, $\bar{\mathbf{g}}$ is given by:

$$\bar{\mathbf{g}} = \begin{cases}\mathbf{g} & \psi \text{ is isometric} \\ \begin{pmatrix}\mathbf{e}_1^\top \\ \mathbf{e}_2^\top\end{pmatrix}\begin{pmatrix}\lambda_1 & \lambda_4 & \lambda_5 \\ \lambda_4 & \lambda_2 & \lambda_6 \\ \lambda_5 & \lambda_6 & \lambda_3\end{pmatrix}\begin{pmatrix}\mathbf{e}_1 & \mathbf{e}_2\end{pmatrix} & \text{otherwise}\end{cases} \tag{48}$$

The CS $\mathbf{\Gamma}_{mn}^p$ at $\mathcal{M}_1$ are given by:

$$\mathbf{\Gamma}_{mn}^p = \frac{1}{2}\mathbf{g}^{pl}\left(\mathbf{g}_{lm,n} + \mathbf{g}_{ln,m} - \mathbf{g}_{mn,l}\right) \tag{49}$$

where $\mathbf{g}_{lm,n} = \partial_n\mathbf{g}_{lm}$ and $\mathbf{g}^{mn} = (\mathbf{g}_{mn})^{-1}$. Using equation (48) in the expressions of CS given in the equation above, $\bar{\mathbf{\Gamma}}_{mn}^p$ at $\mathcal{M}_2$ can be written as:

$$\begin{aligned}\bar{\mathbf{\Gamma}}_{mn}^p &= \frac{1}{2}\bar{\mathbf{g}}^{pl}\left(\bar{\mathbf{g}}_{lm,n} + \bar{\mathbf{g}}_{ln,m} - \bar{\mathbf{g}}_{mn,l}\right) \\ &= \frac{1}{2}\mathbf{g}^{pl}\left(\mathbf{g}_{lm,n} + \mathbf{g}_{ln,m} - \mathbf{g}_{mn,l}\right) = \mathbf{\Gamma}_{mn}^p\end{aligned} \tag{50}$$

Therefore, CS at $\mathcal{M}_1$ and $\mathcal{M}_2$ are preserved under an isometric deformation. For any other deformation, $\bar{\mathbf{\Gamma}}_{mn}^p$ cannot be expressed in terms of $\mathbf{\Gamma}_{mn}^p$ without involving λ_i which are unknown and do not cancel out. Due to this, the preservation of CS for the deformation models other than isometry is not possible.

APPENDIX B
MANIFOLDS AND SURFACES

In general, a manifold is a topological space that resembles the Euclidean space $\mathbb{R}^n$ locally. Therefore, at each point of the manifold one can find a neighborhood that is homeomorphic to the Euclidean space of dimension n. 2D manifolds represent surfaces. If embedded in 3D, they represent 3D surfaces.

B.1 Image Projection

A surface is mathematically related to an image with an image projection function. Figure 13 shows a surface $\mathcal{M} \in \mathbb{R}^3$ being projected into the image $\mathcal{I} \in \mathbb{R}^2$ with the function $\Pi : \mathbb{R}^3 \to \mathbb{R}^2$. We model projection with the perspective camera, where Π takes as input the point $\mathbf{z} = \begin{pmatrix}z^1 & z^2 & z^3\end{pmatrix}^\top$ on the surface $\mathcal{M}$ and outputs its retinal coordinates $\mathbf{x} = \begin{pmatrix}x^1 & x^2\end{pmatrix}^\top$ in the image:

$$\mathbf{x} = \begin{pmatrix}x^1 & x^2\end{pmatrix}^\top = \Pi(\mathbf{z}) = \begin{pmatrix}\frac{z^1}{z^3} & \frac{z^2}{z^3}\end{pmatrix}^\top. \tag{51}$$

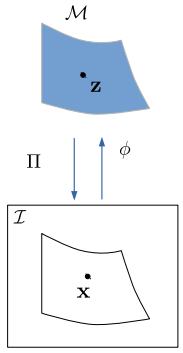

Fig. 13: An image embedding ϕ that relates the 3D surface $\mathcal{M}$ with its image $\mathcal{I}$.

B.2 Image Embedding

The image embedding, denoted as $\phi : \mathcal{I} \to \mathcal{M}$ in figure 13, represents the inverse of Π restricted to the surface $\mathcal{M} \in \mathbb{R}^3$, as it maps retinal coordinates to the 3D surface. It must satisfy the following identity:

$$\mathbf{x} = (\Pi \circ \phi)(\mathbf{x}). \tag{52}$$

Smooth functions that comply with equation (52) can be expressed with a depth function $\rho \in C^\infty(\mathcal{I}, \mathbb{R})$, where:

$$\phi(\mathbf{x}) = \rho(\mathbf{x})\begin{pmatrix}\mathbf{x} & 1\end{pmatrix}^\top. \tag{53}$$

Alternatively, let $\beta = \rho^{-1}$ be the inverse-depth function. This allows us to re-define the image embedding in equation (53) as:

$$\phi(\mathbf{x}) = \frac{1}{\beta(\mathbf{x})}\begin{pmatrix}\mathbf{x} & 1\end{pmatrix}^\top. \tag{54}$$

where β is a function that represents the inverse of the depth of the surface at a point $\mathbf{x} = (x^1, x^2)$ in $\mathcal{I}$. A point on the surface $\mathcal{M}$ is given by:

$$\mathbf{z} = \phi = \beta^{-1} \begin{pmatrix} x^1 & x^2 & 1 \end{pmatrix}^\top. \tag{55}$$

For general surfaces, β is a non-linear function but for planar surfaces it is linear.

APPENDIX C
DIFFERENTIAL K-FORM

A differential k-form represents a smooth section on the infinitesimal tangent space of the manifold. For example, a 0-form describes a point on the manifold, 1-form describes a line element, 2-form describes an area element, 3-form describes a volume element, and so on.

In differential geometry, differential forms (Cartan, 1970; O'Neill, 2006) are used to perform the multivariate calculus independently of the coordinates. A scalar function f, parametrized with m variables $(x^1, x^2, \dots x^m)$ such that a point $\mathbf{z} = f(x^1, x^2, \dots x^m)$ is a 0-form. In this case, the exterior derivative of f is the same as the total derivative of f.

Now, the differential 1-form expressing the exterior derivative of f is given by:

$$\mathrm{d}\mathbf{z} = \sum_{t=1}^{m} \frac{\partial f}{\partial x^t} \mathrm{d}x^t, \tag{56}$$

where $\mathrm{d}x^t$ are the 1-forms and $\dfrac{\partial f}{\partial x^t}$ represents a linear function on the tangent space of the function f in $\mathbb{R}^n$.

Differential forms are defined locally, in terms of the local coordinates. Hence they are easily transferable from one coordinate system to another and therefore, very useful for defining local properties of the surfaces.

APPENDIX D
FORMULATION OF DEFORMATION MODELS USING METRIC TENSORS AND MOVING FRAMES

Given the moving frames $(\mathbf{e}_1, \mathbf{e}_2, \mathbf{e}_3)$ at $\mathcal{M}_1$ and $(\bar{\mathbf{e}}_1, \bar{\mathbf{e}}_2, \bar{\mathbf{e}}_3)$ at $\mathcal{M}_2$ in figure 12, the metric tensors $\mathbf{g}$ and $\bar{\mathbf{g}}$ at $\mathcal{M}_1$ and $\mathcal{M}_2$ are given by:

$$\mathbf{g} = \mathbf{J}_f^\top \mathbf{J}_f = \begin{pmatrix} \mathbf{e}_1^\top \mathbf{e}_1 & \mathbf{e}_1^\top \mathbf{e}_2 \\ \mathbf{e}_2^\top \mathbf{e}_1 & \mathbf{e}_2^\top \mathbf{e}_2 \end{pmatrix} \quad \bar{\mathbf{g}} = \mathbf{J}_g^\top \mathbf{J}_g = \begin{pmatrix} \bar{\mathbf{e}}_1^\top \bar{\mathbf{e}}_1 & \bar{\mathbf{e}}_1^\top \bar{\mathbf{e}}_2 \\ \bar{\mathbf{e}}_2^\top \bar{\mathbf{e}}_1 & \bar{\mathbf{e}}_2^\top \bar{\mathbf{e}}_2 \end{pmatrix}. \tag{57}$$

The four categories of deformation models shown in figure 2 are characterized by the following metric tensor and moving frames invariants:

Deformation	*Metric tensor*	*Moving frames*
Isometric	$\mathbf{g} = \bar{\mathbf{g}}$	$\bar{\mathbf{e}}_i^\top \bar{\mathbf{e}}_j = \mathbf{e}_i^\top \mathbf{e}_j \quad i,j \in \{1,2\}$
Conformal	$\mathbf{g} \propto \bar{\mathbf{g}}$	$\bar{\mathbf{e}}_i^\top \bar{\mathbf{e}}_j \propto \mathbf{e}_i^\top \mathbf{e}_j \quad i,j \in \{1,2\}$
Equiareal	$\lvert\mathbf{g}\rvert = \lvert\bar{\mathbf{g}}\rvert$	$\lvert\lvert\bar{\mathbf{e}}_1 \times \bar{\mathbf{e}}_2\rvert\rvert^2 = \lvert\lvert\mathbf{e}_1 \times \mathbf{e}_2\rvert\rvert^2$
Skewless	$\gamma(\mathbf{g}) = \gamma(\bar{\mathbf{g}})$	$\alpha(\mathbf{e}_1, \mathbf{e}_2) = \alpha(\bar{\mathbf{e}}_1, \bar{\mathbf{e}}_2)$

$$\text{where } \gamma(\mathbf{g}) = \frac{\mathbf{g}_{12}^2}{\mathbf{g}_{11}\mathbf{g}_{22}} \text{ and } \alpha(\mathbf{e}_1, \mathbf{e}_2) = \frac{(\mathbf{e}_1^\top \mathbf{e}_2)^2}{\mathbf{e}_1^\top \mathbf{e}_1 \mathbf{e}_2^\top \mathbf{e}_2}. \tag{58}$$

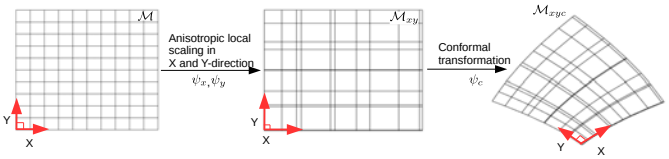

Fig. 14: An example of skewless deformation. A surface grid undergoes anisotropic scaling in two orthogonal directions and then undergoes a conformal transformation. Therefore, only the angles between the basis are preserved.

APPENDIX E
THEOREMS AND THEIR PROOFS

Theorem 1 (Skewless mappings)**.** *A mapping is skewless iff it can be decomposed into a conformal mapping and orthotropic scalings along the orthogonal frame basis.*

Proof. First we prove the reverse implication of the theorem, i.e., anisotropic scalings and a conformal mapping lead to a skewless mapping. In figure 14, we have:

$$\psi_{xyc} = \psi_c \circ \psi_y \circ \psi_x. \tag{59}$$

Since ψ_x and ψ_y are anisotropic local scalings along the orthogonal frame basis, they preserve the angles along the orthonormal frame basis. Therefore, ψ_x, ψ_y and their composition is a skewless mapping. ψ_c is a conformal mapping and therefore, it is skewless too, which makes ψ_{xyc} a skewless mapping.

Note that $\psi_c \circ \psi_y \circ \psi_x$ and $\psi_c \circ \psi_x \circ \psi_y$ are both skewless mappings as the anisotropic scalings are commutative. However, $\psi_x \circ \psi_c \circ \psi_y$ is not a skewless mapping anymore due to the non-commutativity of the conformal mapping.

In order to prove the forward implication, we need to show that a skewless mapping ψ_{xyc} can always be decomposed into a conformal mapping ψ_c and anisotropic local scalings along the orthogonal frame basis.

We can always express ψ_{xyc} as:

$$\psi_{xyc} = \psi_c \circ \psi_y \circ \psi_x \circ \psi_u, \tag{60}$$

where ψ_u is an unknown mapping. On decomposing ψ_{xyc} as in equation (60), we have that $\psi_y \circ \psi_x \circ \psi_u$ must be a skewless mapping. ψ_u cannot be a conformal mapping as it is non-commutative with anisotropic scalings. ψ_u can be expressed as:

$$\psi_u = \psi_{x'} \circ \psi_{y'} \circ \psi_{x'y'}, \tag{61}$$

where $\psi_{x'}$ and $\psi_{y'}$ are transformations along the orthogonal frame basis. $\psi_{x'y'}$ represents a transformation that is not along the orthogonal frame basis and therefore it does not preserve the angles along the orthogonal frame basis.

Therefore $\psi_y \circ \psi_x \circ \psi_u$ can only be a skewless mapping if $\psi_{x'y'}$ is identity. Otherwise, it causes a scaling which is not along the orthogonal frame basis which makes $\psi_y \circ \psi_x \circ \psi_u$ a non-skewless mapping.

Hence a skewless mapping can only be defined as a combination of anisotropic scaling followed by a conformal mapping. Note that the decomposition according to equation (59) is unique upto a scale factor only. □

Theorem 2 (Isometric mappings)**.** *An isometric mapping between two planes preserves the connection forms* $(w_1^1, w_2^1, w_1^2, w_2^2)$.

Proof. Given that $g = \psi \circ f$ in figure 12, the moving frames $(\mathbf{e}_1, \mathbf{e}_2, \mathbf{e}_3)$ and $(\bar{\mathbf{e}}_1, \bar{\mathbf{e}}_2, \bar{\mathbf{e}}_3)$ on the planes $\mathcal{M}_1$ and $\mathcal{M}_2$ are related by:

$$\begin{pmatrix}\bar{\mathbf{e}}_1 & \bar{\mathbf{e}}_2\end{pmatrix} = \mathbf{J}_{\psi\circ f}\begin{pmatrix}\mathbf{e}_1 & \mathbf{e}_2\end{pmatrix} = \begin{pmatrix}\mathbf{J}_{\psi\circ f}\mathbf{e}_1 & \mathbf{J}_{\psi\circ f}\mathbf{e}_2\end{pmatrix}. \quad (62)$$

On differentiating the above equation, we obtain:

$$\begin{pmatrix}\mathrm{d}\bar{\mathbf{e}}_1 & \mathrm{d}\bar{\mathbf{e}}_2\end{pmatrix} = \mathbf{J}_{\psi\circ f}\begin{pmatrix}\mathrm{d}\mathbf{e}_1 & \mathrm{d}\mathbf{e}_2\end{pmatrix} + \mathrm{d}\mathbf{J}_{\psi\circ f}\begin{pmatrix}\mathbf{e}_1 & \mathbf{e}_2\end{pmatrix}. \quad (63)$$

Since ψ is an isometric mapping between two planes, $\mathbf{J}_{\psi\circ f} = \mathbf{R}$, where $\mathbf{R}$ is a rotation matrix and therefore we have $\mathrm{d}\mathbf{J}_{\psi\circ f} = 0$ in the previous equation. We multiply the two expressions obtained in the above equation with $\bar{\mathbf{e}}_1^\top$ and expand the expression using the connection relations $\mathrm{d}\mathbf{e}_t = w_t^1\mathbf{e}_1 + w_t^2\mathbf{e}_2$. We obtain:

$$\begin{aligned}\bar{w}_1^1\bar{\mathbf{e}}_1\bar{\mathbf{e}}_1^\top + \bar{w}_1^2\bar{\mathbf{e}}_2\bar{\mathbf{e}}_1^\top &= \mathbf{J}_{\psi\circ f}\left(w_1^1\mathbf{e}_1 + w_1^2\mathbf{e}_2\right)\bar{\mathbf{e}}_1^\top \\ \bar{w}_2^1\bar{\mathbf{e}}_1\bar{\mathbf{e}}_1^\top + \bar{w}_2^2\bar{\mathbf{e}}_2\bar{\mathbf{e}}_1^\top &= \mathbf{J}_{\psi\circ f}\left(w_2^1\mathbf{e}_1 + w_2^2\mathbf{e}_2\right)\bar{\mathbf{e}}_1^\top.\end{aligned} \quad (64)$$

We employ equation (62) and rewrite the above expression as:

$$\begin{aligned}\bar{w}_1^1\bar{\mathbf{e}}_1\bar{\mathbf{e}}_1^\top + \bar{w}_1^2\bar{\mathbf{e}}_2\bar{\mathbf{e}}_1^\top &= w_1^1\bar{\mathbf{e}}_1\bar{\mathbf{e}}_1^\top + w_1^2\bar{\mathbf{e}}_2\bar{\mathbf{e}}_1^\top \\ \bar{w}_2^1\bar{\mathbf{e}}_1\bar{\mathbf{e}}_1^\top + \bar{w}_2^2\bar{\mathbf{e}}_2\bar{\mathbf{e}}_1^\top &= w_2^1\bar{\mathbf{e}}_1\bar{\mathbf{e}}_1^\top + w_2^2\bar{\mathbf{e}}_2\bar{\mathbf{e}}_1^\top.\end{aligned} \quad (65)$$

Since $(\bar{\mathbf{e}}_1, \bar{\mathbf{e}}_2)$ are linearly independent, on expressing w_t^s in terms of $\Gamma_{tk}^s \mathrm{d}x^k$ in the above equation we obtain $\bar{\Gamma}_{tk}^s = \Gamma_{tk}^s$ and therefore, $\begin{pmatrix}\bar{w}_1^1 & \bar{w}_2^1 & \bar{w}_1^2 & \bar{w}_2^2\end{pmatrix} = \begin{pmatrix}w_1^1 & w_2^1 & w_1^2 & w_2^2\end{pmatrix}$. □

Theorem 3 (Linear mappings)**.** *A linear mapping between two planes preserves the connection forms* $(w_1^1, w_2^1, w_1^2, w_2^2)$.

Proof. Given that $g = \psi \circ f$ in figure 12, the moving frames $(\mathbf{e}_1, \mathbf{e}_2, \mathbf{e}_3)$ and $(\bar{\mathbf{e}}_1, \bar{\mathbf{e}}_2, \bar{\mathbf{e}}_3)$ on the planes $\mathcal{M}_1$ and $\mathcal{M}_2$ are related by equation (62), which on differentiation leads to equation (63). Since ψ is a linear mapping, we have $\mathrm{d}\mathbf{J}_{\psi\circ f} = 0$. Following the same procedure as theorem 2, one can easily show that the connections forms are also preserved in this case. □

Theorem 4 (Non-solvability of Equiareal NRSfM)**.** *Equiareal NRSfM is not locally solvable.*

Proof. The constraint in equiareal mappings is given by:

$$\begin{aligned}&\frac{EG}{k^4} - \frac{F}{k^4}^2 = \frac{\bar{E}\bar{G}}{\bar{k}^4} - \frac{\bar{F}^2}{\bar{k}^4} \\ &\frac{\partial}{\partial\bar{x}^i}\left(\frac{\bar{E}}{\bar{k}^2}\right)\frac{\bar{G}}{\bar{k}^2} + \frac{\bar{E}}{\bar{k}^2}\frac{\partial}{\partial\bar{x}^i}\left(\frac{\bar{G}}{\bar{k}^2}\right) - 2\frac{\bar{F}}{\bar{k}^2}\frac{\partial}{\partial\bar{x}^i}\left(\frac{\bar{F}}{\bar{k}^2}\right) = \\ &\left(\frac{\partial}{\partial x^1}\left(\frac{E}{k^2}\right)\frac{\partial x^1}{\partial\bar{x}^i} + \frac{\partial}{\partial x^2}\left(\frac{E}{k^2}\right)\frac{\partial x^2}{\partial\bar{x}^i}\right)\frac{G}{k^2} \\ &+ \left(\frac{\partial}{\partial x^1}\left(\frac{G}{k^2}\right)\frac{\partial x^1}{\partial\bar{x}^i} + \frac{\partial}{\partial x^2}\left(\frac{G}{k^2}\right)\frac{\partial x^2}{\partial\bar{x}^i}\right)\frac{E}{k^2} \\ &- 2\frac{F}{k^2}\left(\frac{\partial}{\partial x^1}\left(\frac{F}{k^2}\right)\frac{\partial x^1}{\partial\bar{x}^i} + \frac{\partial}{\partial x^2}\left(\frac{F}{k^2}\right)\frac{\partial x^2}{\partial\bar{x}^i}\right), \quad i \in \{1, 2\}\end{aligned} \quad (66)$$

Without IP, these expressions are in terms of β, $\bar{\beta}$ and their first and second-order derivatives. Using IL, we obtain the following constraints:

$$\begin{aligned}\bar{k}_1 &= \frac{\partial x^1}{\partial\bar{x}^1}k_1 + \frac{\partial x^2}{\partial\bar{x}^1}k_2 - \frac{\partial\bar{x}^2}{\partial x^1}\frac{\partial^2 x^1}{\partial\bar{x}^1\bar{x}^2} - \frac{\partial\bar{x}^2}{\partial x^2}\frac{\partial^2 x^2}{\partial\bar{x}^1\bar{x}^2} \\ \bar{k}_2 &= \frac{\partial x^1}{\partial\bar{x}^2}k_1 + \frac{\partial x^2}{\partial\bar{x}^2}k_2 - \frac{\partial\bar{x}^1}{\partial x^1}\frac{\partial^2 x^1}{\partial\bar{x}^1\bar{x}^2} - \frac{\partial\bar{x}^1}{\partial x^2}\frac{\partial^2 x^2}{\partial\bar{x}^1\bar{x}^2}.\end{aligned} \quad (67)$$

Using this constrain in equation (66), it results in 7 variables (β, $\bar{\beta}$ and the first and second-order derivatives of β) in 3 equations. This system is not solvable. Even if we differentiate equation (66) further, it always results in higher number of variables than equations.

Under IP, the simplified constraint is given by:

$$\begin{aligned}&\det\mathbf{J}_\eta\left(\bar{k}_1 - \left(k_1\frac{\partial x^1}{\partial\bar{x}^1} + k_2\frac{\partial x^2}{\partial\bar{x}^1}\right)\right) = \\ &-\frac{\partial x^2}{\partial\bar{x}^2}\frac{\partial^2 x^1}{\partial\left(\bar{x}^1\right)^2} + \frac{\partial x^2}{\partial\bar{x}^1}\frac{\partial^2 x^2}{\partial\left(\bar{x}^1\right)^2} + \frac{\partial x^2}{\partial\bar{x}^1}\frac{\partial^2 x^1}{\partial\bar{x}^1\partial\bar{x}^2} - \frac{\partial x^1}{\partial\bar{x}^1}\frac{\partial^2 x^2}{\partial\bar{x}^1\partial\bar{x}^2} \\ &\det\mathbf{J}_\eta\left(\bar{k}_2 - \left(k_1\frac{\partial x^1}{\partial\bar{x}^2} + k_2\frac{\partial x^2}{\partial\bar{x}^2}\right)\right) = \\ &-\frac{\partial x^2}{\partial\bar{x}^2}\frac{\partial^2 x^1}{\partial\bar{x}^1\partial\bar{x}^2} + \frac{\partial x^2}{\partial\bar{x}^1}\frac{\partial^2 x^2}{\partial\bar{x}^1\partial\bar{x}^2} + \frac{\partial x^2}{\partial\bar{x}^1}\frac{\partial^2 x^1}{(\partial\bar{x}^2)} - \frac{\partial x^1}{\partial\bar{x}^1}\frac{\partial^2 x^2}{(\partial\bar{x}^2)}.\end{aligned} \quad (68)$$

Using equation (67) in this constraint leads to expressions independent of $(\bar{k}_1, \bar{k}_2)$ and (k_1, k_2). Therefore, it is not solvable. Differentiating equation (68) to find more constraints under the assumption of IP does not make sense as it contradicts the assumption of IP. Hence, we show that the PDE (66) for equiareal NRSfM does not possess a local solution. □

Corollary 1 (Isometric mappings under IP)**.** *Under IP, an isometric mapping between two non-planar surfaces preserves the connection forms* $(w_1^1, w_2^1, w_1^2, w_2^2)$.

Proof. Given that $g = \psi \circ f$ in figure 12, the moving frames $(\mathbf{e}_1, \mathbf{e}_2, \mathbf{e}_3)$ and $(\bar{\mathbf{e}}_1, \bar{\mathbf{e}}_2, \bar{\mathbf{e}}_3)$ on the surfaces $\mathcal{M}_1$ and $\mathcal{M}_2$ are related by equation (62). On differentiating equation (62), we obtain equation (63). Since ψ is an isometric mapping, under IP $\mathbf{J}_{\psi\circ f} = \mathbf{R}$. Therefore $\mathrm{d}\mathbf{J}_{\psi\circ f} = 0$. Following the same procedure as theorem 2, one can easily show that the connections forms are also preserved in this case. □

Corollary 2 (Infinitesimally linear mappings)**.** *An IL mapping between two surfaces preserves the connection forms* $(w_1^1, w_2^1, w_1^2, w_2^2)$.

Proof. Given that $g = \psi \circ f$ in figure 12, the moving frames $(\mathbf{e}_1, \mathbf{e}_2, \mathbf{e}_3)$ and $(\bar{\mathbf{e}}_1, \bar{\mathbf{e}}_2, \bar{\mathbf{e}}_3)$ on the surfaces $\mathcal{M}_1$ and $\mathcal{M}_2$ are related by equation (62). On differentiating equation (62), we obtain equation (63). Since ψ is an IL mapping, it is point-wise linear. Therefore $\mathrm{d}\mathbf{J}_{\psi\circ f} = 0$. Following the same procedure as theorem 3, one can easily show that the connections forms are also preserved in this case. □

APPENDIX F
RESULTS

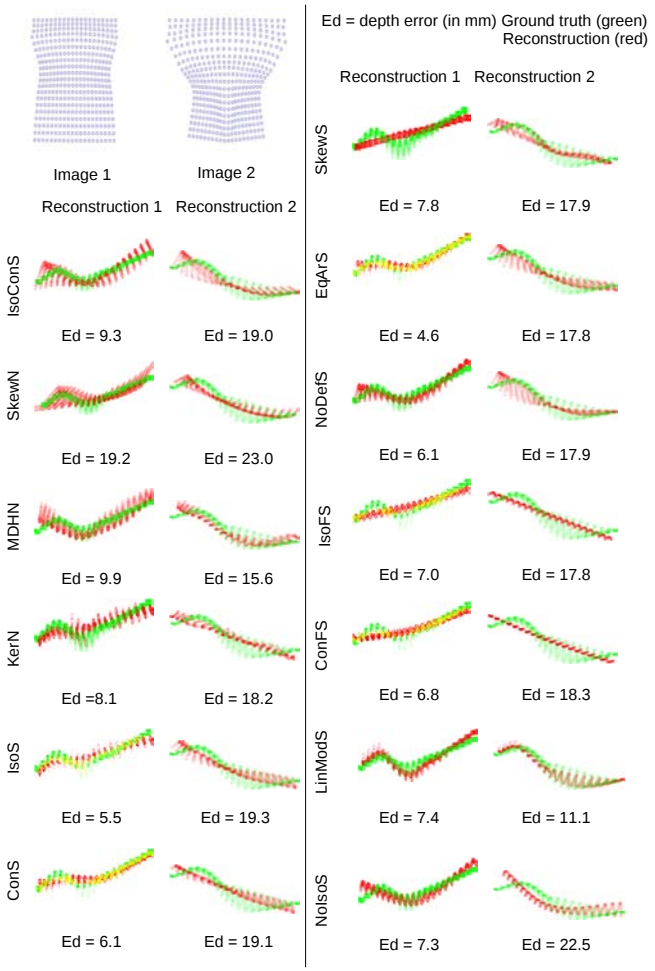

Fig. 15: Reconstructions for surfaces 10 and 20 from the rubber dataset. The second image shows the maximum stretch of the rubber. The depth error maps show the difference in the reconstruction and ground truth. Best viewed in colour.

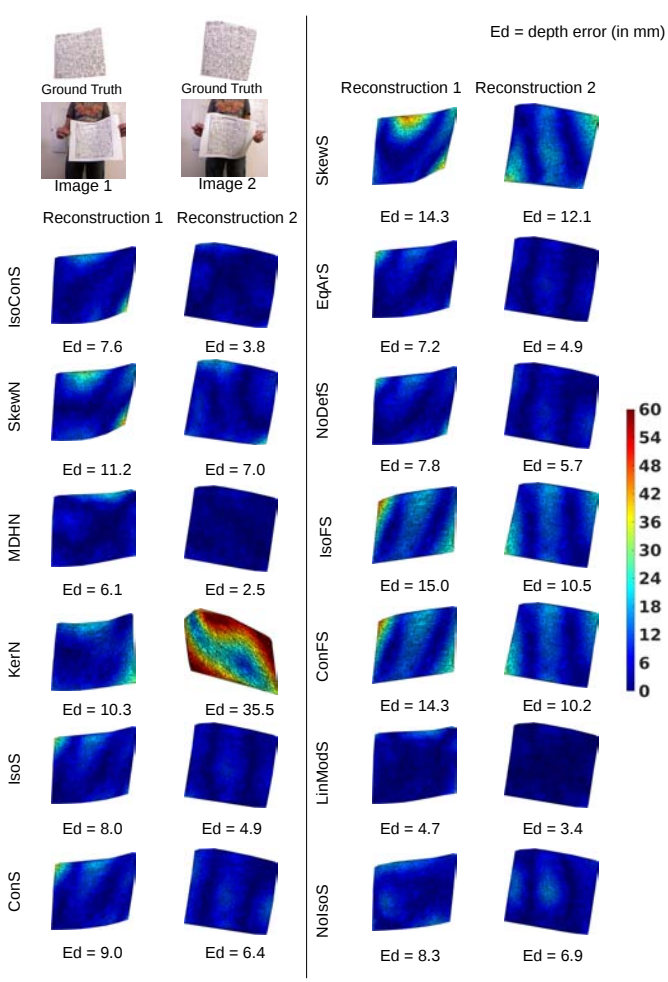

Fig. 16: Error maps for two surfaces of the paper dataset. The depth error maps show the difference in the reconstruction and ground truth. Best viewed in colour.

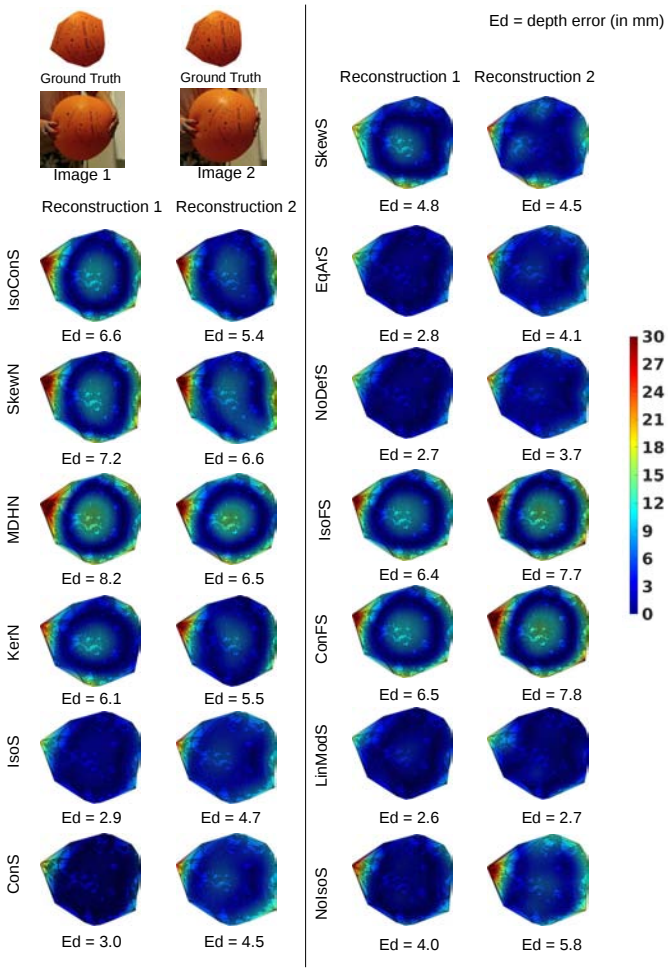

Fig. 17: Error maps for two surfaces of the balloon dataset. The depth error maps show the difference in the reconstruction and ground truth. Best viewed in colour.

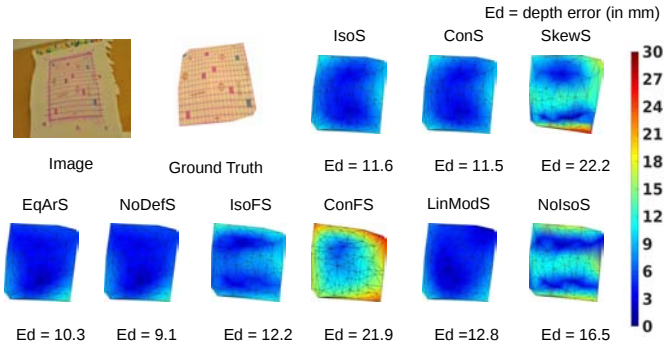

Fig. 18: Error maps of reconstruction from all SfT methods of the tissue dataset. Best viewed in colour.